Metal organic framework derived Ni-S/C catalysts for selective alkyne hydrogenation

Ning Li,[1,2,δ] Shaoxia Weng,[1,2,δ] Alan J. McCue,[3] Yuanfei Song,[1,2] Yufei He,[1,2]

Yanan Liu,[1, 2,*] Junting Feng,[1,2] Dianqing Li[1, 2, *]

[1]*State Key Laboratory of Chemical Resource Engineering, Beijing Engineering Center for Hierarchical Catalysts, Beijing University of Chemical Technology, Beijing, 100029, China*

[2] *Quzhou Institute for Innovation in Resource Chemical Engineering, Quzhou, 324000, China*

[3] *Department of Chemistry, University of Aberdeen, Aberdeen AB24 3UE, U.K.*

* Corresponding author

Address: Box 98, 15 Bei San Huan East Road, Beijing 100029, China

Tel: +86 10 64436992 Fax: +86 10 64436992

E-mail: ynliu@mail.buct.edu.cn (Yanan Liu); lidq@mail.buct.edu.cn (Dianqing Li)

[δ] These two authors contribute equally

ABSTRACT

A carbon matrix supported Ni catalyst with surface/sub-surface S species is prepared using a sacrificial metal organic framework synthesis strategy. The resulting highly dispersed Ni-S/C catalyst contains surface discontinuous and electron-deficient $Ni^{\delta+}$ sites modified by p block S elements. This catalyst proved to be extremely active and selective for alkyne hydrogenation. Specifically, high intrinsic activity (TOF=0.0351 s^{-1}) and superior selectivity (>90%) at complete conversion was achieved. Whereas, an analogous S free sample prepared by same synthetic route performed poorly. That is, the incorporation of S in Ni particles and carbon matrix exerts a remarkable positive effect on catalytic behavior for alkyne hydrogenation, with breaking the activity-selectivity trade-off. Through comprehensive experimental studies, enhanced performance of Ni-S/C was ascribed to the presence of

discontinuous Ni ensembles which promote desorption of weakly π-bonded ethylene and an optimized electronic structure modified via obvious p-d orbitals hybridization.

KEYWORDS: MOF-derived metal catalysts; S modified Ni particles; S-doped carbon matrix; Isolated $Ni^{\delta+}$-S sties; Selective acetylene hydrogenation

1. INTRODUCTION

Selective catalytic hydrogenation of acetylene impurities in an ethylene rich stream is an important industrial process in the production of the polyethylene feedstock[1,2]. With the increasingly urgent societal requirement for green chemical processes, more stringent requirements have been put forward for producing polymer-grade ethylene in which the acetylene content must be reduced to < 1 ppm[3,4]. Consequently, the efficient hydrogenation of acetylene into ethylene has become a key challenge in catalysis. Pd-based catalysts are considered as the most active materials at present and are thus widely used for this reaction industrially under mild reaction conditions[5]. However, in recent years, the precious metal prices have risen continuously[6]. Based on this, it is highly desirable to find alternatives for Pd catalysts preferably based on earth-abundant and low-cost metals.

Along this line, Ni-based catalysts have attracted considerable attention for selective acetylene hydrogenation since the metals unfilled d electron orbital leads to an ability to dissociate hydrogen[7,8]. However, monometallic Ni catalysts suffer from poor selectivity towards the target ethylene product due to a combination of over-hydrogenation and oligomerization of acetylene to form 1,3-butadiene as a precursor to green oil which builds up on the catalyst leading to deactivation (Note: this latter effect is especially prominent at high conversion levels required to achieve < 1 ppm alkyne concentration)[9]. Evidence demonstrates that modification of the geometric structure and electronic properties of Ni can significantly enhance ethylene desorption limiting over hydrogenation[10,11]. There is also evidence that when a p-block heteroatom occupies an interstitial site in a metal nanoparticle this can be advantageous in terms of regulating surface structures and altering adsorption

properties of reactants[12,13]. For example, the addition of C atoms into the interstitial sites in Pd or Ni_3Zn particles contributed to a shift in d-band center of active metal towards Fermi level and inhibited the formation of a subsurface hydrogen species, with both improving ethylene selectivity[14,15]. Similarly, introduction of B atoms into the interstitial site of a Pd catalyst modified the electronic structure of active centers[16]. The p-block sulfur element is also known as an excellent structural modifier for supported metal catalysts and may even limit aggregation of an active metal species if introduced into the support.[17,18] Our previous experimental results[19] showed that metal sulfides were highly effective for alkyne hydrogenation since the sulfide phase lead to the formation of uniform discontinuous metal sites (i.e., metal atom ensemble size was limited by the presence of S but in a regular manner based on the underlying metal sulfide crystal structure). However, in many cases improved ethylene selectivity is achieved at the expense of activity[20]. Consequently, managing this activity-selectivity trade-off still remains challenging to date.

Metal Organic Frameworks (MOF) are a class of ordered porous polymers composed of metal ions/clusters and organic ligands acting as linkers. MOFs in their own right are interesting catalytic materials as a result of the high surface area and diverse structures that can form[21,22]. Alternatively, a MOF can be used as a sacrificial precursor through a pyrolysis process. In other words, by tuning the MOF and pyrolysis process, MOF-derived nanomaterials with specific desired composition, structure and enhanced stability can be readily obtained[23,24]. For instance, researchers applied Ni/Co atoms as the nodes to prepare MOFs as a structure directing template. By inducing pyrolysis, highly dispersed and stable metal nanoparticles were supported on carbon substrate with properties that exceeded what was possible from traditional impregnation or immobilization[25]. Moreover, heteroatoms such as N or P can also be introduced into MOF structure and potentially become incorporated in the pyrolysis derived catalyst[26]. Inspired by this, we herein explore the possibility of preparing Ni-MOF-derived catalysts with/without p block S element and probe the role of S in enhancing catalytic properties for alkyne hydrogenation. After direct

carbonization of a Ni-S-MOF at relatively low temperature, S-doped carbon supported Ni-S species was formed. When compared with a sulfur-free Ni/C catalysts derived from the same parent Ni-MOF, the S containing sample offered considerably better selectivity and activity. Based on detailed characterization results, both the electronic state and geometric structure of active Ni species is shown to be regulated by p-block characteristics of guest S into both the active metal and the support.

2. EXPERIMENTAL DETAIL

2.1 Synthesis of precursors and catalysts

Firstly, a pristine Ni-MOF precursor was successfully prepared through a hydrothermal approach. In detail, 1.45 g of $Ni(NO_3)_2 \cdot 6H_2O$ and 0.83 g of 1,4-benzenedi-carboxylic acid (H_2BDC) were dissolved in 60 mL of DMF with the aid of ultrasound for 10 min. Then, the obtained solution was poured into a 100 mL Teflon-lined stainless autoclave and heated to 120 ℃ for 15 h. The solid products were collected by centrifugation and washed using DMF and anhydrous ethanol to remove any residual reactant, followed by drying at 60 ℃ for 12 h. The resulting material is denoted as 'Ni-MOF' throughout. Subsequently, 1.00 g of Ni-MOF and 5 mL DMSO were dispersed in 20 mL of anhydrous methanol and then stirred at room temperature for 12 h. The resulting solid was collected by centrifugation and washed with anhydrous ethanol and then dried at 60 ℃ for 12 h. This material is denoted as 'Ni-S-MOF' throughout. The Ni-MOF and Ni-S-MOF materials were then heated for 2 h at 300 ℃ in 10 vol.% H_2/N_2 with flow rate of 55 mL/min using the fix-bed micro-reactor to obtain the supported metal catalysts, denoted as 'Ni/C' and 'Ni-S/C'. Synthesis of contrast samples was shown in Supporting Information.

2.2 Catalyst testing

Catalytic behavior was evaluated in a fix-bed micro-reactor at atmospheric pressure. In detail, 0.1 g of catalysts and 1.4 g quartz sand (Aldrich, 40-70 mesh) were mixed and reduced at 300 ℃ for 2 h in 10 vol% H_2/N_2 flow before cooling to below 70 ℃ in N_2 atmosphere. Subsequently, the reaction was carried out using a feed gas mixture of 0.45% C_2H_2/0.91% H_2/45.00% C_2H_4/1.00% C_3H_8/N_2 as balance with a space velocity

of 13200 h^{-1}. The detail analysis method of reactant and product concentrations was shown in Supporting Information.

2.3 Catalyst characterization

X-ray Absorption Spectroscopy (XAS) were performed at 1W1B beamline of the National Synchrotron Radiation Light Source II at the Beijing Synchrotron Radiation Facility. The samples were preserved in N_2 atmosphere to prevent re-oxidation in air and then measured in transmission mode. The typical energy of the stored ring was 2.5 GeV and the maximum current was 250 mA. Data were collected in transmission mode using a Si (111) bicrystal monochromator with an ionization chamber. In situ Diffuse Reflectance Infrared Fourier Transform Spectroscopy (DRIFTS) reactions were performed using a Bruker Tensor II instrument. The catalysts were first pretreated with 10.0 vol% H_2/N_2 at 300 ^oC for 2 h, before a background spectrum was collected at a resolution of 4 cm^{-1}. After cooling to 25 °C under Ar flow, 5.0 vol% C_2H_2/N_2 and 10.0 vol% H_2/N_2 were introduced and the sample temperature increased incrementally to 200°C. H_2-D_2 exchange experiments were performed in a fixed-bed reactor with an on-line mass spectrometer (Hiden EXQ). Typically, 0.10 g of sample was reduced in H_2 at 300 °C for 2 h (flow rate = 20 mL/min) and then cooled to room temperature in Ar stream. Then, 10% H_2/N_2 and 99.99% D_2 with flow rate of 20 mL/min, respectively was introduced. After the baseline of the mass spectrometer had stabilized, the signals of H_2, HD and D_2 were collected as temperature was from 20 ^oC to 60°C with 5 °C intervals. The details of other characterizations were shown in Supporting Information.

3. RESULTS AND DISCUSSION

3.1 Synthesis and structure of MOF-derived Ni-based catalysts

The stepwise synthesis of p-block S element modified Ni/C catalyst begins with a Ni-based MOF (denoted as Ni-MOF) fabricated through a hydrothermal method[27]. Ni-MOF was then exposed to S source (DMSO) to yield Ni-S-MOF and subsequently used as a sacrificial template. An analogous material was also prepared from same Ni-

MOF but without S introduction, named Ni/C throughout. Powder X-ray Diffraction (XRD) analysis was initially implemented to gain insight into the crystalline structure and phase throughout the synthesis process. As presented in Figure 1A, the pristine Ni-MOF presents some strong diffraction peaks, the position of which are basically consistent with the simulated theoretical patterns (CCDC 851688)[28], thus confirming the initial hydrothermal synthesis is successful.

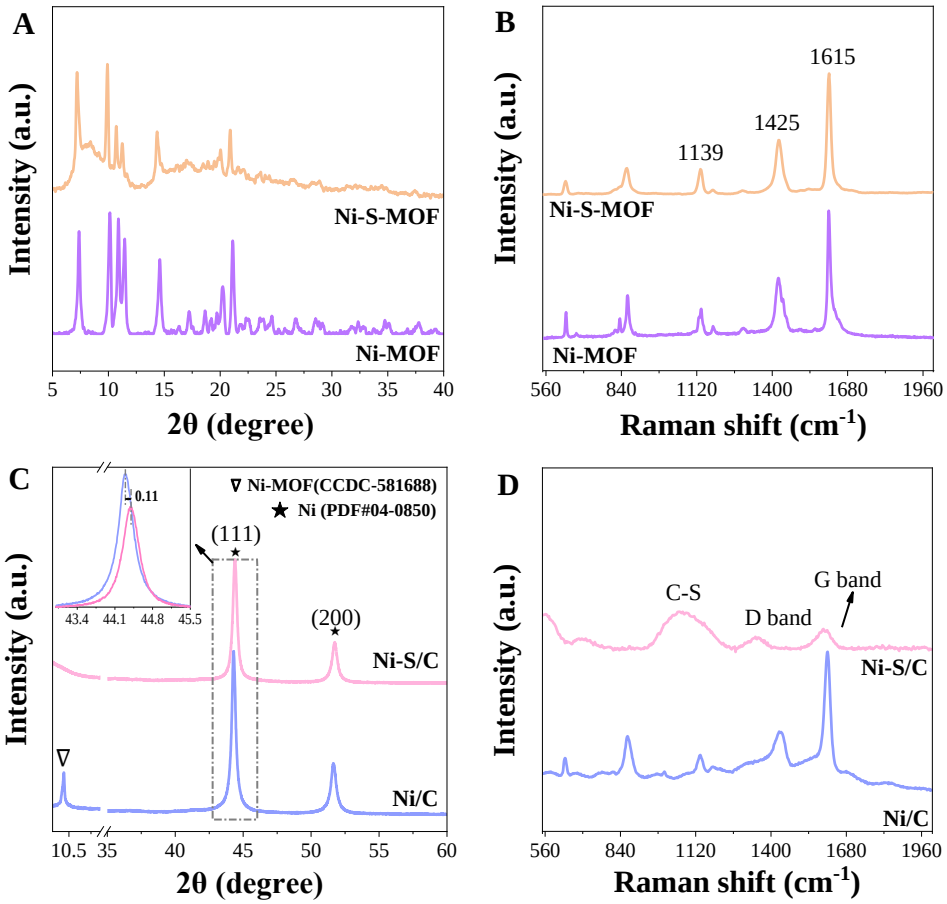

Figure 1. The preparation and structural characterizations of Ni catalysts. (A, B) XRD patterns and Raman spectra of Ni-MOF and Ni-S-MOF; (C, D) XRD patterns and Raman spectra of Ni-S/C and Ni/C samples.

After introducing p-block S element, same diffraction peaks are observed, suggesting the underlying Ni-MOF structure remains, albeit the crystallinity of the Ni-MOF decreases with some humps appearing likely as a result of the steric constraints originating from the bulky $(CH_3)_2$-S-O (as S source) molecules[29]. Raman spectra (Figure 1B) further reveal the pristine Ni-MOF structure. Specifically, the low

wavenumber peaks (626 & 862 cm^{-1}) are assigned to C-H stretching vibrations and bands at 1139, 1425 & 1615 cm^{-1} are attributed to -COOH group coupled with C-C stretching and a benzene ring stretching vibration[30]. These observations are also consistent with FTIR spectra (see Figure S1). Furthermore, pyrolysis led to the recovery of a carbon supported Ni-based catalyst. Based on the modulation at different temperature (Figure S2-S4), 300 °C for pyrolysis is selected to obtain a MOF-derived catalysts. XRD patterns of Ni-S/C and Ni/C samples are shown in Figure 1C. The diffraction patterns of the underlying MOF structure disappear without other peaks being observed for Ni-S/C because of the structure collapse, while the characteristic of MOF still could be observed in Ni/C at 8.8-9.3° possibly suggesting the original structure is partially preserved. There is no evidence of diffraction peaks associated with a crystalline carbon phase and this is likely associated with the low pyrolysis temperature meaning graphitic carbon can't form[31]. However, instead diffraction peaks associated with metallic fcc-Ni appear at 44.5° (111) and 51.8° (200) (PDF#04-0850), thus confirming the generation of Ni nanoparticles. There is a subtle difference between Ni/C and Ni-S/C samples though - Ni peak intensity is lower in S-containing sample. Furthermore, the diffraction peaks show a small upshift of 0.11° for Ni-S/C (see inset in Figure 1C). According to Bragg's law, the shift could be ascribed to lattice strain suggesting that S may have inserted into Ni lattice during pyrolysis and hence occupies either interstitial sites. However theoretically, the insertion of S should expand the lattice and result in a downshift of the peak. As such, the observed upshift appears somewhat counterintuitive and may require further exploration[32]. The transformation described above could be also confirmed by Raman and FTIR results (Figure 1D and S5) where the vibrations characteristic of MOF precursor is seen to disappear for Ni-S/C and partially disappear/weaken for Ni/C. Raman spectra of Ni-S/C also exhibits new vibrations. Two broad peaks around 1280-1420 and 1540-1660 cm^{-1} appear, assigned to D and G band of amorphous carbon support[33]. Importantly, a band at 1080 cm^{-1} is consistent with a C-S bond stretching vibration[34], indicative of S doped carbon

support (i.e., by combining insight from XRD and Raman spectroscopy it appears that S may be associated with both Ni nanoparticles and C support). Given that S-doped carbon has been shown to stabilize metal nanoclusters, it might be that there is a link between weaker Ni diffraction peaks for Ni-S/C (Figure 1C) [18].

The microstructure of two synthesized catalysts were further explored by HRTEM-EDX measurements. The images presented in Figure 2A show the existence of amorphous carbon layers after pyrolysis of MOF precursor consistent with Raman spectra described earlier. By observing several different regions, it can be noted that Ni nanoparticles are homogeneously dispersed in Ni-S/C without observation of any larger Ni aggregates (average size = 7.7 ± 0.1 nm, Table S1). In contrast, Ni particle size for Ni/C is notably larger (average = 10.0 ± 0.2 nm; Figure 2C). Based on the study by Yin et al.[18], it was found that the incorporation of S into carbon matrix was helpful for enhancing metal dispersion, responsible for more exposed active sites for S modified Ni-based catalysts. Indeed, Ni-S/C also exhibits higher dispersion of 16.8% than Ni/C (11.6%). At high magnification (Figure 2D) lattice fringes with a spacing of 0.203 nm are detected for Ni/C corresponding to Ni (111). However interestingly lattice spacing of 0.199 nm are observed for Ni-S/C (Figure 2B), which does not specifically correspond to that of Ni (111), nor correlate with any well-defined nickel sulfide phase. Given that the spacing of 0.199 nm is close to metallic Ni and Ni peak shift observed from XRD (see earlier), it can be reasonably inferred that sulfur atoms enter into Ni lattice and locate at interstitial sites (denoted as S-IS Ni). Moreover, EDX elemental mapping demonstrates that there is a high degree of correlation between S and Ni located on C which helps to support our interpretation (Figure S6). Notably, S:Ni ratio of 0.121 determined from EDX closely matches that determined by ICP-AES analysis (0.125). Interestingly, the equivalent S:Ni ratio derived from XPS is 0.133. Whilst XPS ratio is only slightly higher, it is considered that the technique accounts for S & Ni in the surface and near surface region only.

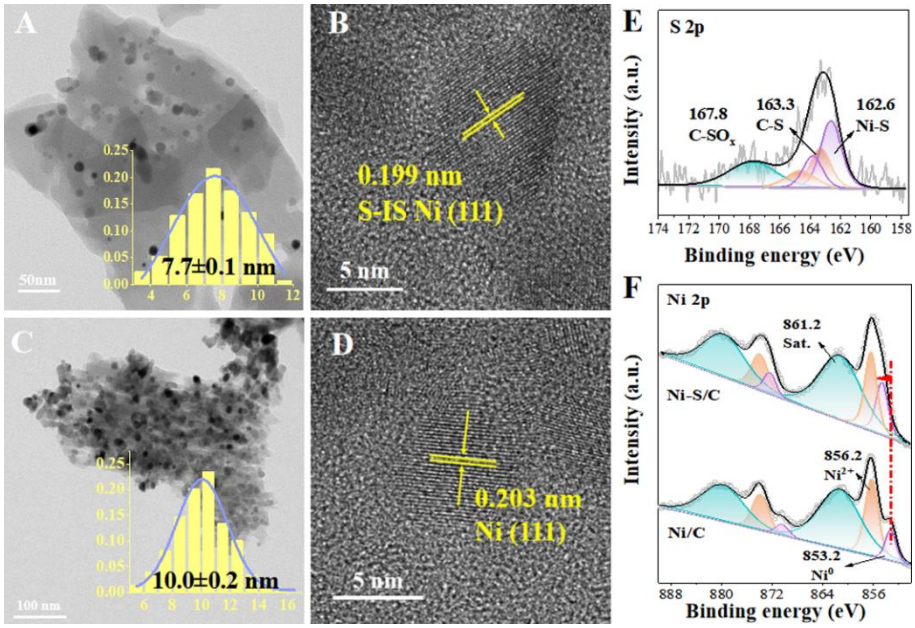

Figure 2. Characterizations of geometric and electronic structure over Ni catalysts. (A, B) HRTEM images Ni-S/C at different scales with size distribution and observed lattice spacing (C, D) HRTEM images at different scales of Ni/C catalysts with Ni particle size distribution and observed lattice spacing; High-resolution XP spectra of (E) S 2p (F) Ni 2p of Ni catalysts.

In order to obtain more information about surface state of Ni-S/C catalyst, DRIFT measurements were carried out using CO as probe molecule. Figure 3A shows a strong band appears at 2046 cm^{-1} (linearly-adsorbed CO) for Ni-S/C along with a weaker band at ca. 1880 cm^{-1} (multi-bonded CO), suggesting that the most common adsorption site is discontinuous Ni ensembles diluted by S atoms [35]. Similarly, this interpretation is also confirmed by EXAFS analysis, where a notable peak appears in the region of 1−2 Å (Figure 3B-C), but the intensity is significantly lower than that of NiO reference, ascribed to a Ni-S contribution with a fitted bond length of 2.17 Å[36]. This suggests that the presence of S could dilute Ni ensemble on the surface such that smaller clusters of Ni can exist and is consistent with a significant reduction in Ni-Ni coordination number and increase in the apparent Ni-Ni interatomic distance[37] (Table S2). However in sharp contrast, Ni/C catalyst without S doping only shows bands at 1920-1830 cm^{-1} ascribed to the multi-bound CO on the Ni ensembles[38,39]. Therefore, it seems reasonable to assume that S present in Ni-S/C is essentially concentrated on

or near surface. Indeed, it has been previously reported that low concentrations of S atoms have a tendency to migrate to the surface[40].

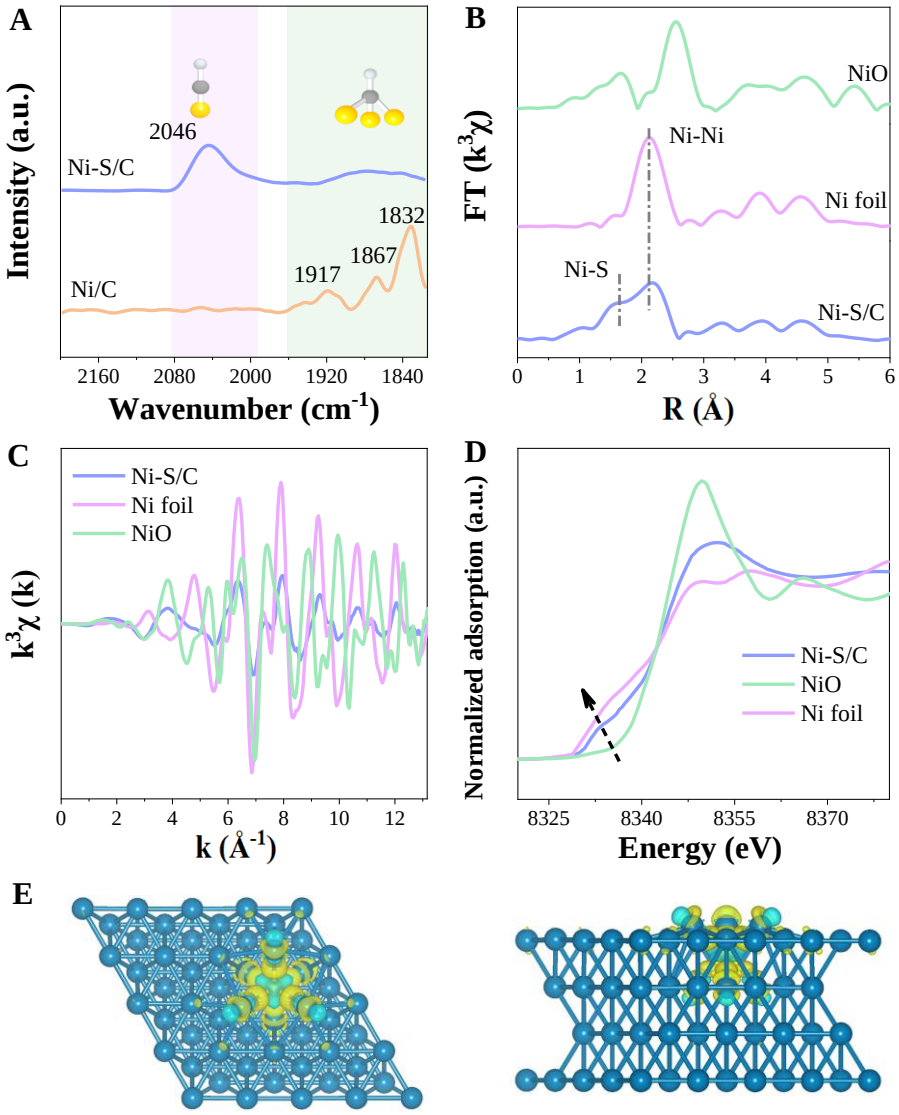

Figure 3. The characterization of the fine structure of nickel catalysts. (A) FTIR spectra of CO adsorption over Ni-S/C and Ni/C samples; (B, C) FT-EXAFS spectra and fitting curve of k^3-weighted Ni K-edge EXAFS oscillations; (D) Normalized XANES spectra for Ni-S/C with NiO and Ni foil as reference; (E) Differential charge density of the heteroatom-doped Ni (111) surfaces. Yellow and cyan shadow regions represent the charge accumulation and deletion, respectively. The values of absolute iso-surfaces are 0.004 e·Å^{-3}.

To directly understand the electronic interaction between the host Ni and the guest S due to the strong hybridization, XANES spectra are given in Figure 3D along with

Ni foil and NiO for reference. The near-edge lines in Ni-S/C samples are similar to those of Ni foil, but located at somewhat higher energy (between Ni foil and NiO), indicating that Ni species is in an electron-deficient state. Also, XPS spectra were collected (Figure 2 and S7) and deconvoluted with fixed FWHM for the same species in each sample using a 70%/30% Gaussian/Lorentzian sum. Error bars of the peak-fitting parameters were determined as 95% confidence intervals. For Ni-S/C sample, the deconvoluted peak for S 2p at 162.6 and 163.8 eV are ascribed to a typical metal-S bond[41], while the peaks at 163.3 and 164.7 eV are assigned to a C-S bond[42] (Figure 2E). The latter is well agreement with the result from C1s XPS spectra (Figure S7). Additionally, the peak at 167.8 eV would ordinarily be attributed to S in an oxidized state – possibly a SO_x type species[43]. These spectral assignments would then be consistent with the interpretation that S is associated with both the active metal species and carbon support[44]. S binding energy appears to differ from S-doped C reported in literature [45] (BE shift for S $2p_{3/2}$ and S $2p_{1/2}$ in Ni-S/C of 0.4 eV) which further emphasizes the dual role of S as the shift would be indicative of S existing in an electron-enriched state – presumably from donation from Ni (i.e., there is a Ni-S contribution and C-S contribution).

As expected for the corresponding Ni 2p XP spectra of Ni-S/C (Figure 2F) gives the characteristic peaks of a metallic Ni at 853.2 and 870.4 eV[46], and oxidized Ni^{2+} species at 856.2 and 873.8 eV[47]. The appearance of the latter stems from re-oxidation of Ni species in air during storage and testing process. Notably, the peak position originating from Ni species at 854.6 eV is dominant in the Ni-S/C, higher than that of Ni/C, implying that the electronic configuration of Ni interacting with S forms a $Ni^{\delta+}$ species. Diffusion of S atoms into interstitial sites of Ni lattice is also investigated using DFT calculations with the most favorable configuration for a sulfur atom on Ni (111) facets summarized in Figure S8. Notably, sulfur atom preferentially adsorb on tetrahedral interstices on the subsurface for Ni (111) which affects the charge density of Ni species via p-d orbitals hybridization. As displayed in Figure 3E, Ni atom loses electrons and p block S element gains electrons, in line with the previous report as

well as more electronegative S than Ni. Bader charge of Ni atom in S-Ni (111) is 0.54e, suggesting that the penetrated heteroatom evidently modifies the charge of surface Ni atoms as positive owing to the lattice contraction induced by S doped into the subsurface. Overall, all the above observations confirm the complex role of S within Ni-S/C sample with S incorporation into Ni particles resulting in dilution of Ni ensemble size along with electron transfer to yield a $Ni^{0.54+}$ species. Furthermore, S also appears to dope into carbon matrix which enhances Ni dispersion.

3.2 Catalytic evaluation in acetylene hydrogenation

The resulting Ni-S/C material was then utilized for selective hydrogenation of acetylene in an ethylene enriched stream to evaluate catalytic performance in a lab-scale fixed-bed reactor (H_2:C_2H_2 = 2:1). Results are then compared to Ni/C sample for benchmarking. Note that for industrial acetylene hydrogenation the preferred reaction set-up involves only a small excess of hydrogen as this helps limit over-hydrogenation[48]. For Ni based catalysts, a larger excess of hydrogen is typically required to limit deactivation from oligomer formation[49,50]. As shown in Figure 4A, Ni-S/C sample achieves complete acetylene conversion at a reaction temperature of 178 °C. In contrast, Ni/C sample displays a volcano type relationship as a function of reaction temperature with acetylene conversion increasing to *ca*. 50% at 140 °C before rapidly decreasing due to the deactivation (see later). This therefore suggests that whilst Ni-S/C and Ni/C show similar activity at low temperature, this is not true at higher temperatures where Ni-S/C sample is undoubtedly more active (and presumably more stable). Ni-MOF as comparison is further treated at higher temperature to obtain the similar Ni content relative to Ni-S/C catalyst. However, the as-prepared Ni/C at high temperature also displays a volcano type relationship as a function of reaction temperature with acetylene conversion increasing to *ca*. 40% at 180 °C before rapidly decreasing (Figure S9). Activity of Ni-S/C is even comparable to catalytic activity of Ni/Al_2O_3 prepared by a conventional impregnation but only when Al_2O_3 sample is tested with a 20-fold excess of H_2 relative to acetylene (Figure S10). In terms of selectivity, the incorporation of p block S elements (Figure 4B)

results in high selectivity to ethylene with only a small amount of ethane or oligomer formation. Importantly, the excellent ethylene selectivity (90.9%) remains at complete acetylene conversion with 6.1% ethane and 3.0% oligomer. At full conversion, you would ordinarily expect to see a drop off in selectivity (Figure S11) since ethylene is free to adsorb and react. With Ni-based catalysts, it is also common to see a marked increase in oligomer formation at high conversion when hydrogen availability is lower. Neither appears to happen over Ni-S/C catalyst described here. For Ni/C as benchmarking, it is true that ethylene selectivity is high at low acetylene conversion. However, as temperature increases beyond 140 °C (Figure 4C), the generation of green oil (originating from coupling processes of C_2 species) increases markedly (more than 10%) which in turn leads to the observed deactivation. One additional point that is worthy of mention is what happens to the apparent ethylene selectivity during deactivation – it remains high and this is related to conversion (Figure S12).

To further prove the advantages of Ni-S/C fabricated from a MOF precursor, performance was compared with a nickel sulfide sample prepared by an impregnation method. Sulfide phase in this case was characterized as the Ni_3S_2 phase and whilst the S: Ni ratio differs from the Ni-S/C sample, this ratio does represent the most sulfur deficient phase expected from a typical Ni-S phase diagram[51]. As shown in Figure S13 and Table S3, the introduction of guest S to form nickel sulfide is helpful in terms of selectivity but this comes at the expense of activity. More specifically, when a Ni_3S_2/Al_2O_3 sample is tested with the same 2:1 H_2:C_2H_2 ratio used for Ni-S/C a reaction temperature of 370 °C is needed to obtain 59% reactant conversion vs 160 °C for Ni-S/C. The activity of Ni_3S_2/Al_2O_3 sample can be compensated for by increasing H_2:C_2H_2 ratio to 20 and operating with a far low space velocity such that complete conversion can be achieved at lower temperature but at the expense of selectivity (see Table S3). All in all, the above observations suggest that Ni-S/C sample offers unique catalytic behavior, even with an unusually low H_2/C_2H_2 ratio for Ni-based catalysts and this must be related to the presence of S. Indeed, when compared with the most

state-of-the-art non-noble metal catalysts previously reported Ni-S/C is both highly active and selective (see Figure S14 and Table S4).

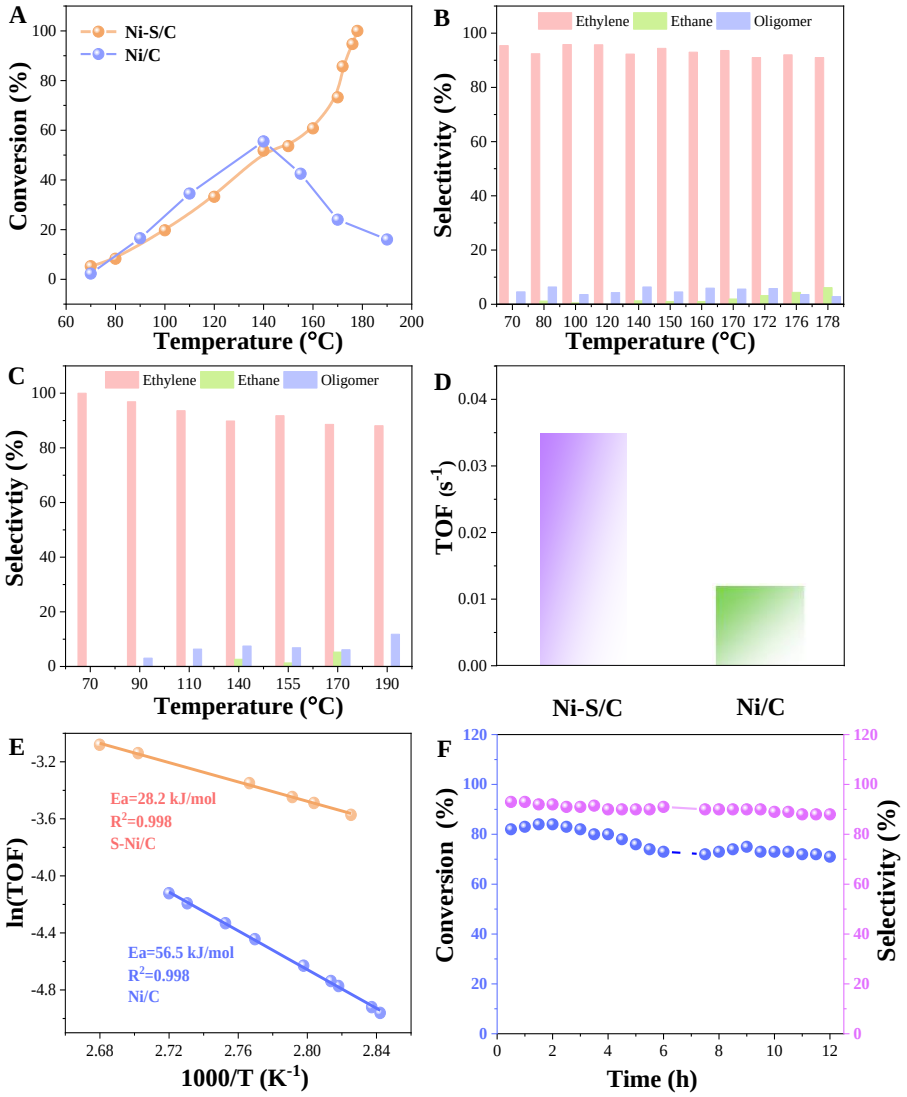

Figure 4. Catalytic behavior in selective acetylene hydrogenation. (A) Acetylene conversion as a function of temperature; Selectivity to ethylene, ethane and oligomer as a function of temperature over (B) Ni-S/C (C) Ni/C (reaction conditions: 0.1 g of catalyst, 2:1 of H_2/C_2H_2, total flow = 218 mL min^{-1}, SV = 13200 h^{-1}); (D) TOF (E) Arrhenius plots of Ni catalysts (F) Long-term stability for Ni-S/C at 165 °C for 720 min.

The intrinsic activity of Ni catalyst was calculated from data obtained under kinetic control (i.e., in the absence of heat/mass transfer limitations-see Supporting Information and Table S5). TOF of Ni-S/C is 0.0351 s^{-1}, 3 times higher than that of

Ni/C at 88 °C (Figure 4D). Moreover, from an Arrhenius plot the apparent activation energies were calculated as 28.2 kJ/mol for Ni-S/C and 56.5 kJ/mol for Ni/C (Figure 4E). Both TOF and E_a values further demonstrate the high activity of sulfur containing catalyst. The differences in selectivity to C_4^+ products for these two catalysts suggests that higher stability should be expected for Ni-S/C catalyst. To explore this aspect, a longer time period reaction is performed at 165 ^oC (temperature chosen to ensure that any deactivation could be observed). From Figure 4F, Ni-S/C catalyst gives the satisfactory stability over a 720 min period. Acetylene conversion is seen to decrease (80 → 70%) whereas ethylene selectivity remains close to 90% throughout, being basically in agreement with TG data. From Figure S15, a small weight loss (ca. 10%) was observed at 270 ^oC corresponding to the decomposing of a relatively harmless carbonaceous species, confirmed by the maintained activity of this sample after coke was removed (Figure S16). These results indicate that whilst S modified sample is inherently more stable, small selectivity to oligomers will still have an impact, albeit on a much longer timescale as compared to Ni/C.

3.3 Origin of enhancement for catalytic performance

The acetylene hydrogenation reaction is a structure-sensitive reaction, with smaller size facilitates to enhance the catalytic behavior[52]. Consequently, Ni-S/C catalysts with smaller particle size exhibits higher activity. Also, well known that the adsorption energy of reactants plays a crucial role in catalysis with too strong or too weak an interaction adversely affecting catalytic activity or influencing selectivity. With regards to acetylene hydrogenation, a moderate adsorption strength is considered key[53]. Accordingly, a valence-band XPS study was conducted to measure d-band electronic states, as this directly links with the adsorbate bonding affinity on the active sites and is a good descriptor of the adsorbate-metal interaction. Interestingly, d-band center of Ni shifts towards Fermi level in the presence of S implying a positive shift of d center toward the unoccupied 3d band of Ni (Figure 5A). As such, this gives a proper filling degree of anti-bonding orbital, thermodynamically beneficial for hydrogen activation and ethylene desorption, thus improving catalytic performance.

To understand how Ni particle structure influences adsorption behavior, in situ DRIFTS analysis of pre-adsorbed propyne as the probe molecule was carried out at increasing temperature since acetylene does not give rise to particularly strong IR bands due to its symmetry. As shown in Figure S17 and S18, the peaks at 1350-1567 cm^{-1}, identified as ≡C–H bond vibration[54], and the bands at 2080-2180 cm^{-1}, corresponding to C≡C stretching vibration are observed, indicative of adsorbed alkyne. Noted that the band intensity decreases significantly on Ni-S/C as temperature increases from 20 to 140 °C. In contrast, little change is apparent over Ni/C even when heating to 160 °C. The above difference may be attributed to the difference in catalyst structure. It is thought that the alkyne is weakly π-adsorbed on Ni-S/C and this may be linked with the presence of discontinuous Ni sites (i.e., S acts to dilute Ni surface such that smaller clusters of Ni can exist - consistent with CO-IR analysis), whereas in the absence of S, Ni catalyst permits more strongly bound multi-σ-bonded alkyne, being in line with the measured reaction order with respect to acetylene.

Figure 5B shows a plot of intrinsic activity versus C_2H_2 pressure which gives a good straight line fit with reaction orders of -0.6 for Ni/C and 0.1 for Ni-S/C. A negative C_2H_2 reaction orders indicates that the reaction rate is suppressed by strong acetylene adsorption on Ni[55]. As reported previously[56], the weakly π-absorbed intermediates are readily hydrogenated to produce a vinyl intermediate leading to excellent hydrogenation performance. H_2-D_2 isotope exchange experiments were performed to gain further insight into the activation of H_2 on Ni-S/C and Ni/C. S containing sample shows immediate HD generation at low temperature in a H_2-D_2 flow (Figure 5C), whereas HD formation over Ni/C catalyst is less apparent (Figure 5D) which broadly correlates with catalytic activity. One justification for higher ethylene selectivity is more energetically favored desorption relative to further hydrogenation. To verify this experimentally, C_2H_4-TPD measurements were conducted. To distinguish between desorption of C_2H_4 and loss/decomposition of S/C from the catalyst a separate thermogravimetric experiment was performed under N_2 flow (Figure S19) – as such, only desorption in the range of 50-350 °C is attributable to chemisorbed species.

From C_2H_4-TPD data in Figure 5E, Ni/C displays a sharp desorption feature centered at 310 °C, previously assigned to desorption from strongly σ-bonded C_2H_4 bridging between Ni sites and multi-σ-bonded bound to hollow Ni sites[10]. In sharp contrast, Ni-S/C shows are far broader desorption peak centered at 180 °C, confirming ethylene is adsorbed weaker which correlates with the catalytic data.

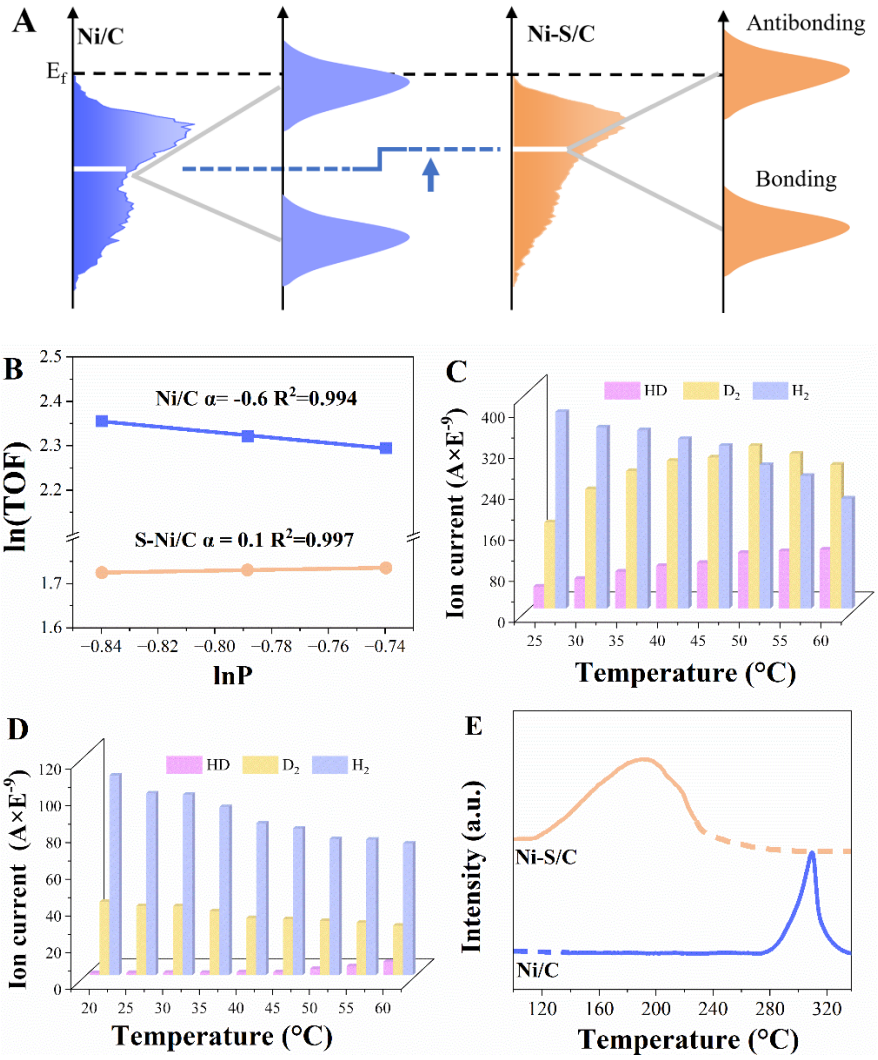

Figure 5. Study of structure-performance relationship. (A) Valence band XPS spectra (B) Reaction order with respect to acetylene; H_2-D_2 isotope exchange at various temperatures for (C) Ni-S/C (D) Ni/C (E) C_2H_4-TPD profiles.

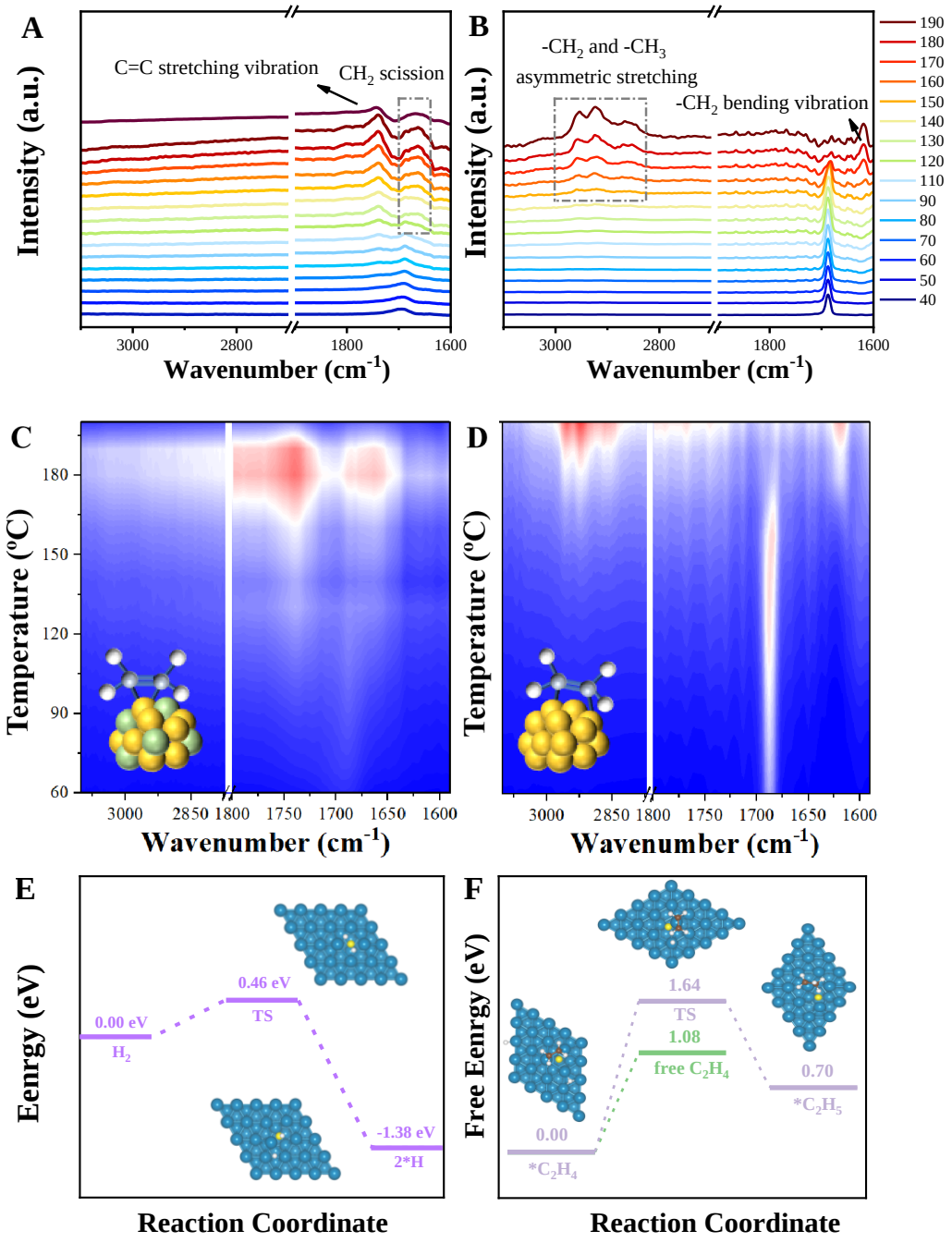

Figure 6. The adsorption property of reactants. In-situ DRIFTS spectra of the hydrogenation of co-adsorbed acetylene with H_2 at elevated temperatures (A, C) Ni-S/C (B, D) Ni/C catalysts. The assignments of the characteristic peaks are schematically shown in the insets above the spectra. Energy profiles for (E) the dissociation of H_2 at Ni-S surfaces (F) the barriers of further hydrogenation and desorption energy of C_2H_4* intermediate.

Acetylene hydrogenation was further investigated *in-situ* DRIFTS by increasing temperature from 40 to 190 °C (Figure 6A and 6B). Characteristic bands associated with CH_2 scission and C=C stretching vibrations appear at 1637 and 1729 cm^{-1} consistent with the ethylene generation on Ni-S/C catalyst. Notably, the peaks increase in intensity as temperature is increased, however no noticeable bands appear in C-H stretching region (3000-2800 cm^{-1}) suggesting little ethane and oligomers formation – again consistent with earlier catalytic tests. These demonstrate the weaker adsorption of ethylene and the suppressed generation of ethane as well as oligomers over S modified Ni/C catalyst (Figure 6C). However, on Ni/C catalyst, bands at 2933 and 2968 cm^{-1} are apparent and become more intense with increasing temperature consistent with more facile oligomer formation on Ni in the absence of S (Figure 6D). DFT calculation was further conducted to gain a fundamental understanding of the role of S atoms occupying the interstitial sites of Ni lattice for the selective hydrogenation. We first compare the dissociation of H_2 on Ni (111) surface with S modification. Interestingly, H_2 could be activated by S atom, and both H atoms are adsorbed on S atom with the activation barrier of 0.46 eV (Figure 6E), implying a lower energy process relative to that on Ni (111) previously reported with the energy barrier of H_2 dissociation of 0.8 eV[57]. Final state exhibits H atom being anchored on a sulfur atom, while the other one on Ni atom. This illustrates that H_2 heterolytic dissociation by Ni and S is dominant, also accounting for the preferable activity. The occupancy of the interstitial S atoms could suppress hydride species at the same sites to reduce undesirable over-hydrogenation. This is further supported by the comparison on the barriers of further hydrogenation over adsorbed C_2H_4* intermediate to ethane and desorption energy of C_2H_4 product, in which the former (1.64 eV) is much higher than the latter (1.08 eV), responsible for high selectivity (Figure 6F).

Spent catalysts were then analyzed to gain insight into higher stability of Ni-S/C versus Ni/C. The mean size of spent Ni-S/C increases marginally relative to fresh one (7.7 ± 0.1 vs 8.1 ± 0.2 nm) but this is very close to not being statistically significant.

Ni particles also remain homogeneously dispersed on the support after longer reaction periods (Figure S20). However, sintering is apparent for the sulfur free catalyst (fresh 10.0 ± 0.2 nm vs used 11.6 ± 0.2 nm; Figure S21). Increased stability for Ni-S/C is attributed to S role within the support acting to protect against metal agglomeration. Given that deactivation of Ni during acetylene hydrogenation is commonly attributed to carbon retention, XRD patterns were collected after use as shown in Figure S22. Ni/C sample exhibits a pronounced diffraction peak at 2θ=27.5°assigned to the characteristic (002) facets of C (PDF 75-1621) because of carbon deposition or the support becoming more crystalline (note: the support is considered amorphous before the reaction). A similar peak is observed for Ni-S/C but with far weaker intensity. Raman spectra collected on used Ni-S/C look very similar to fresh sample (Figure 1D vs S23), however for Ni/C there is a difference. The peak intensity ratio for D band vs G band increases after use. That is to say, a more ordered graphitic carbonaceous species may be generated and retained on Ni surface, blocking the active sites more effectively. These data sets help to further explain the excellent stability of Ni-S/C catalyst.

4. Conclusion

In summary, we have successfully fabricated carbon matrix supported Ni-S nanoparticles via pyrolysis of a MOF precursor. Given the simplicity of sacrificial MOF approach and the underlying flexibility of MOFs in general, this represents an interesting route towards carbon supported metal catalysts. Ni/C sample prepared directly from the pristine MOF precursor behaved very much like a traditional supported Ni catalyst for acetylene hydrogenation. Specifically, whilst initially active and selective towards the target ethylene product, the catalyst deactivated because of excessive oligomer formation which led to loss of active sites. In contrast, when p-block S element was introduced into MOF prior to pyrolysis a far different catalytic material was obtained. Through detailed characterization it was determined that S was retained both within carbon support and Ni nanoparticles. S within carbon matrix

appears to facilitate enhanced metal dispersion whilst also limiting sintering. S:Ni ratio within nanoparticles was determined to be far lower than is ordinarily observed for a Ni sulfide phase, however the catalytic performance suggested that Ni surface was best described as being discontinuous (i.e., S acts to break up Ni ensembles) with an electron-deficient Ni species via obvious p-d orbitals hybridization. As-obtained $Ni^{\delta+}$-$S^{\delta-}$ sites exhibited high intrinsic activity (TOF of 0.0351 s^{-1}) and excellent ethylene selectivity of 90.9% even at full acetylene conversion with considerably improved longer term stability relative to Ni/C. Importantly, the impressive catalytic performance was achieved with a low H_2/C_2H_2 ratio which is less common for Ni systems since this ordinarily favors oligomer formation leading to deactivation. Instead, these conditions are more in line with those used for industrial Pd based catalysts. Therefore, this innovative synthesis strategy offers an interesting route to prepare non-noble metal alternatives to Pd for alkyne hydrogenation whilst furthering our understanding of the beneficial role of S for metal catalysis.

AUTHOR INFORMATION

Author Contributions

Ning Li and Shaoxia Weng carried out most of the characterization, structural analysis, and catalytic reactions. Yuanfei Song performed part of the structural analysis. Yanan Liu, Junting Feng, Yufei He and Dianqing Li designed the experiment and provided the funding support. Yanan Liu and Alan McCue discussed the results and wrote the manuscript.

Notes

The authors declare no competing financial interest.

ASSOCIATED CONTENT

Supporting Information

The supporting information is available free of charge at https.

Details include experiment details/methods; FTIR spectra of MOF precursors and Ni-based catalysts; HRTEM images with the corresponding EDX elemental mappings;

High-resolution XPS spectra of C1s; Properties of Ni-S/C catalysts; Catalytic performance of reference Ni/Al_2O_3 and Ni_3S_2/Al_2O_3 catalysts; A comparison of catalytic performance with Ni-based catalysts reported in literatures; Calculations for ruling out the heat and mass transfer limitations; In situ DRIFT spectra of adsorbed alkyne; N_2-TG analysis and HRTEM images of spent catalysts.

ACKNOWLEDGMENTS

This work was financially supported by National Natural Science Foundation of China (22278017), Fundamental Research Funds for the Central Universities (buctrc202303, JD2325) and Young Elite Scientists Sponsorship Program by BAST (No. BYESS2023087).

References

1 Studt, F.; Abild-Pedersen, F.; Bligaard, T.; Sørensen, R. Z.; Christensen, C. H.; Nørskov, J. K. Identification of Non-precious Metal Alloy Catalysts for Selective Hydrogenation of Acetylene. *Science*. **2008**, 320 (5881), 1320−1322.

2 Borodzinski, A.; Bond, G. C.; Selective Hydrogenation of Ethyne in Ethene-Rich Streams on Palladium Catalysts. Part 1. Effect of Changes to the Catalyst during Reaction. *Catal. Rev*. **2006**, 48 (2), 91–144.

3 Zhu, C.; Xu, W.; Liu, F.; Luo, J.; Lu, J.; Li, W. X. Molecule Saturation Boosts Acetylene Semihydrogenation Activity and Selectivity on a Core-Shell Ruthenium@Palladium Catalyst. *Angew. Chem. Int. Ed.* 2023, 62, e202300110.

4 Shi, R.; Wang, Z. P.; Zhao, Y. X.; Waterhouse, G. I. N.; Li, Z.H.; Zhang, B. K.; Sun, Z. M.; Xia, C.; Wang, H. T.; Zhang, T. R. Room-Temperature Electrochemical Acetylene Reduction to Ethylene with High Conversion and Selectivity. *Nat. Catal*. **2021**, 4, 565–574.

5 Huang, F.; Peng, M.; Chen, Y, L.; Cai, X. B.; Qin, X. T.; Wang, N,; Xiao, D, Q.; Jin, L.; Wang, G. Q.; Wen, X. D.; Liu, H. Y.; Ma, D. Low-Temperature Acetylene Semi-Hydrogenation over the Pd_1–Cu_1 Dual-Atom Catalyst. *J. Am. Chem. Soc*. **2022**, 144 (40), 18485−18493.

6 Armbrüster, M.; Kovnir, K.; Friedrich, M.; Teschner, D.; Wowsnick, G.; Hahne, M.;

Gille, P.; Szentmiklosi, L.; Feuerbacher, M.; Heggen, M.; Girgsdies, F.; Rosenthal, D.; Schlogl, R.; Grin, Y. $Al_{13}Fe_4$ as a Low-Cost Alternative for Palladium in Heterogeneous Hydrogenation. *Nat. Mater*. **2012**, 11, 8, 690–693.

7 Chai, Y. C; Wu, G.J; Liu, X. Y; Ren, Y. J; Dai, W. L.; Wang, C. M; Xie, Z. K; Guan, N. J; Li, L. D. Acetylene-Selective Hydrogenation Catalyzed by Cationic Nickel Confined in Zeolite. *J. Am. Chem. Soc*. **2019**, 141 (25), 9920−9927.

8 Li, Z. W.; Zhang, J. P.; Tian, J. M.; Feng, K..; Jiang, Z.; Yan B. H. Unveiling the Origin of Enhanced Catalytic Performance of NiCu Alloy for Semi-Hydrogenation of Acetylene. *Chem. Eng. J*. **2022**, 450, 138244.

9 Liu, Y. N.; Zhao, J. Y.; Feng, J. T.; He, Y. F.; Du, Y. Y.; Li, D. Q. Layered Double Hydroxidederived Ni-Cu Nanoalloy Catalysts for Semi-Hydrogenation of Alkynes: Improvement of Selectivity and Anti-Coking Ability via Alloying of Ni and Cu. *J. Catal*. **2018**, 359, 251–260.

10 Ge, X. H.; Dou, M. Y.; Cao, Y. Q.; Liu, X.; Wen, Q. Y.; Zhang, J.; Qian, G.; Gong, X, Q.; Zhou, X. G.; Chen, L. W.; Yuan, W. K.; Duan, X. Z. Mechanism Driven Design of Trimer Ni_1Sb_2 Site Delivering Superior Hydrogenation Selectivity to Ethylene. *Nat. Commun*. **2022**, 13, 5534.

11 Cao, Y. Q.; Zhang, H.; Ji, S. F.; Sui, Z. J.; Jiang, Z.; Wang, D. S.; Zaera, F.; Zhou, X. G.; Duan, X.Z.; Li, Y. D. Adsorption Site Regulation to Guide Atomic Design of Ni-Ga Catalysts for Acetylene Semi-Hydrogenation. *Angew. Chem*. **2020**, 132, 11744.

12 Teschner, D.; Borsodi, J.; Wootsch, A.; Révay, Z.; Hävecker, M.; Knop-Gericke, A.; Jackson, S. D.; Schlögl, R. The Roles of Subsurface Carbon and Hydrogen in Palladium-Catalyzed Alkyne Hydrogenation. *Science*. **2008**, 320 (5872), 86−89.

13 Yang, Y.; Zhu, X. J.; Wang, L. L.; Lang, J. Y.; Yao, G. H.; Qin, T.; Ren, Z. H,; Chen, L. W.; Liu, X.; Li, W.; Wan, Y. Breaking Scaling Relationships in Alkynol Semi-Hydrogenation by Manipulating Interstitial Atoms in Pd with d-Electron Gain. *Nat. Commun*. **2022**, 13, 2754.

14 Liu, Y. N.; Fu, F. Z.; McCue, A. J; Jones, W.; Rao, D. M.; Feng, J. T.; He, Y. F.; Li, D. Q. Adsorbate-Induced Structural Evolution of Pd Catalyst for Selective Hydrogenation of Acetylene. *ACS Catal*. **2020**, 10 (24), 15048-15059.

15 Niu, Y. M.; Huang, X.; Wang, Y. Z.; Xu, M.; Chen, J. N.; Xu, S. L.; Willinger, M.-G.; Zhang, W.; Wei, M.; Zhang, B. S. Manipulating Interstitial Carbon Atoms in the Nickel Octahedral Site for Highly Efficient Hydrogenation of Alkyne. *Nat. Commun*.

2020, 11, 3324.

16 Chan, C. W. A.; Mahadi, A. H.; Li, M. M. J.; Corbos, E. C.; Tang, C.; Jones, G.; Ku, W. C. H.; Cookson, J.; Brown, C. M.; Bishop, P. T.; Tsang, S. C. E. Interstitial Modification of Palladium Nanoparticles with Boron Atoms as A Green Catalyst for Selective Hydrogenation. *Nat. Commun*. **2014**, 5, 5787.

17 McCue, A. J.; Anderson, J. A. Sulfur as a Catalyst Promoter or Selectivity Modifier in Heterogeneous Catalysis. *Catal. Sci. Technol*. **2014**, 4, 272−294.

18 Yin, P.; Luo, X.; Ma, Y. F.; Chu, S. Q.; Chen, S.; Zheng, X. S.; Lu, J. L.; Wu, X. J.; Liang, H. W. Sulfur Stabilizing Metal Nanoclusters on Carbon at High Temperatures. *Nat. Commun*. **2021**, 12, 3135.

19 Liu, Y. N.; McCue, A. J.; Feng, J. T.; Guan, S. L.; Li, D. Q. Anderson, J. A. Evolution of Palladium Sulfide Phases During Thermal Treatments and Consequences for Acetylene Hydrogenation. *J. Catal*. **2018**, 364, 204–215.

20 McCue, A. J.; Guerrero-Ruiz, A.; Rodríguez-Ramos, I.; Anderson, J. A. Palladium Sulphide - A Highly Selective Catalyst for the Gas Phase Hydrogenation of Alkynes to Alkenes. *J. Catal.* **2016**, 340, 10-16.

21 Stassen, I.; Burtch, N.; Talin, A.; Falcaro, P.; Allendorf, M.; R.Ameloot, R.; An Updated Roadmap for the Integration of Metal–Organic Frameworks with Electronic Devices and Chemical Sensors. *Chem. Soc. Rev*. **2017**, 46, 3185.

22 Feng, L.; Wang, K. Y.; Day, G. S.; Ryder, M. R.; Zhou, H. C. Destruction of Metal−Organic Frameworks: Positive and Negative Aspects of Stability and Lability. *Chem. Rev.* 2020, 120, 13087−13133.

23 Shen, K.; Chen, X. D.; Chen, J. Y.; Li, Y. W. Development of MOF-Derived Carbon-Based Nanomaterials for Efficient Catalysis. *ACS Catal*. **2016**, 6 (9), 5887−5903.

24 Konnerth, H.; Matsagar, B. M.; Chen, S. S.; Prechtl, M. H. G.; Shieh, F. K.; Wu, K. C. W. Metal-Organic Framework (MOF)-Derived Catalysts for Fine Chemical Production. *Coordin. Chem. Rev*. **2020**, 416, 213319.

25 Deibl, N.; Kempe, R. General and Mild Cobalt-Catalyzed C-Alkylation of Unactivated Amides and Esters with Alcohols. *J. Am. Chem. Soc*. **2016**, 138 (34), 10786−10789.

26 Wang, R.; Dong, X. Y.; Du, J.; Zhao, J. Y.; Zang, S. Q. MOF-Derived Bifunctional Cu_3P Nanoparticles Coated by a N, P-Codoped Carbon Shell for Hydrogen Evolution and Oxygen Reduction. *Adv. Mater*. **2018**, 30 (6), 1703711.

27 Song, K. N.; Liang, S. J.; Zhong, X. H.; Wang, M. Y.; Mo, X. F.; Lei, X. Q.; Lin, Z. Tailoring the Crystal Forms of the Ni-MOF Catalysts for Enhanced Photocatalytic CO_2-to-CO Performance. *App. Catal. B Environ*. **2022**, 309, 121232.

28 Wang, P. C.; Meng, F. L.; Liu, C.; Zou, K. Y.; Li, Z. X. A Novel α-Po Interpenetrating Network with Pseudo-Double-Wall pcu Lattices based on the Homoleptic Nickel (II) Node. *Inorg. Chem. Commun*. **2012**, 17, 95-98.

29 Ji, H.; Lee, S.; Park, J.; Kim, T.; Choi, S.; Oh M. Improvement in Crystallinity and Porosity of Poorly Crystalline Metal−Organic Frameworks (MOFs) through Their Induced Growth on a Well-Crystalline MOF Template, *Inorg. Chem*. **2018**, 57, 9048-9054.

30 Liu, Q.; Xie, L. S.; Shi, X. F.; Du, G.; Asiri, A. M.; Luo, Y. L.; Sun, X. P. High-Performance Water Oxidation Electrocatalysis Enabled by a Ni-MOF Nanosheet Array. *Inorg. Chem. Front*. **2018**, 5, 1570-1574.

31 Yin, Y. C.; Liu, X. F.; Wei, X. J.; Yu, R. H.; Shui, J. L. Porous CNTs/Co Composite Derived from Zeolitic Imidazolate Framework: A Lightweight, Ultrathin, and Highly Efficient Electromagnetic Wave Absorber. *ACS Appl. Mater. Inter*. **2016**, 8 (50), 34686-34698.

32 Gilardi, E.; Fabbri, E.; Bi, L.; Rupp, J. L. M.; Lippert, T.; Pergolesi, D.; Traversa, E. Effect of Dopant−Host Ionic Radii Mismatch on Acceptor-Doped Barium Zirconate Micro-Structure and Proton Conductivity, *J. Phys. Chem. C* **2017**, 12, 9739-19747.

33 Pang, H.; Wang, X. Q.; Zhang, G. L.; Chen, H.; Lv, G. H.; Size Yang, S. Characterization of Diamond-Like Carbon Films by SEM, XRD and Raman Spectroscopy. *Appl. Surf. Sci.* **2010**, 256, 6403–6407.

34 Ye, C.; Jiao, Y.; Chao, D. L.; Ling, T.; Shan, J. Q.; Zhang, B. W.; Gu, Q. F.; Davey, K.; Wang, H. H.; Qiao, S. Z. Electron-State Confinement of Polysulfides for Highly Stable Sodium–Sulfur Batteries. *Adv. Mater*. **2020**, 32 (12), 1907557.

35 Huang, C. M.; Zhang, Y. M.; Han, D. M.; He, B. B.; Sun, X. Y.; Liu, M, Y.; Mei, Y.; Yun, Z. Small-Sized Ni Nanoparticles Embedded Nickel Phyllosilicate as a Metal-Acid Bifunctional Zeolite Catalyst for Cooperatively Boosting CO_2-CH_4 Reforming. *Fuel*. **2023**, 331, 125957.

36 Hong, Y. R.; Mhin, S.; Kim, K. M.; Han, W. S.; Choi, H.; Ali, G.; Chung, K. Y.; Lee, H. J.; Moon, S. I.; Dutta, S.; Sun, S.; Jung, Y. G.; Song, T.; HyukSu Han, H. Electrochemically Activated Cobalt Nickel Sulfide for an Efficient Oxygen Evolution Reaction: Partial Amorphization and Phase Control. *J. Mater. Chem. A.* **2019**, 7, 3592.

37 Luo, Y. T.; Qin, J. H.; Yang, G. X.; Luo, S.; Zhao, Z. M.; Chen, M.; Ma, J. T. N-Ni-S Coordination Sites of NiS/C_3N_4 Formed by an Electrochemical-Pyrolysis Strategy for Boosting Oxygen Evolution Reaction. *Chem. Eng. J.* **2021**, 410, 128394.

38 Mejía, C. H.; Jessi, E. S. Hoeven, V. D.; Petra, E.; Jongh, D. Jong, K. P. D. Cobalt–Nickel Nanoparticles Supported on Reducible Oxides as Fischer–Tropsch Catalysts. *ACS Catal*. **2020**, 10 (13), 7343-7354.

39 Richard, A. R.; Fan, M. H. Low-Pressure Hydrogenation of CO_2 to CH_3OH using Ni-In-Al/SiO_2 Catalyst Synthesized via a Phyllosilicate Precursor. *ACS Catal.* **2017**, 7 (9), 5679-5692.

40 Takeuchi, A.; Tanaka, K. I.; Toyoshima, I.; Miyahara, K. Catalysis and Coordinative Unsaturation of Active Sites on Sulfurated Nickel Catalyst: I. Reversible Formation of Active Sites for Partial Hydrogenation of Acetylene. *J. Catal*. **1975**, 40 (1), 94−100.

41 Yu, J.; Zhang, T.; Xing, C. C.; Li, X. J.; Li, X. Y.; Wu, B.; Li, Y. Enhanced Oxygen Evolution Catalytic Activity of NiS_2 by Coupling with Ferrous Phosphite and Phosphide**.** *Sustain. Energ. Fuels*. **2021**, 5, 1801-1808.

42 Liu, Y. L.; Luo, X. H.; Zhou, C. L.; Du, S.; Zhen, D. S.; Chen, B.; Li, J.; Wu, Q.; Iru, Y.; Chen, D. C. A Modulated Electronic State Strategy Designed to Integrate

Active HER and OER Components as Hybrid Heterostructures for Efficient overall Water Splitting. *Appl. Catal. B: Environ*. **2020**, 260, 118197.

43 Zhang, Y. Y.; Wang, X.; Hu, D. D.; Xue, Z.; Wang, W.; Yang, H. J.; Li, D.S.; Wu, T. Monodisperse Ultrasmall Manganese-Doped Multimetallic Oxysulfide Nanoparticles as Highly Efficient Oxygen Reduction Electrocatalyst. *ACS Appl. Mater. Inter*. **2018,** 10 (16), 13413-13424.

44 Cao, F. F.; Zhao, M. T.; Yu, Y. F.; Chen, B.; Huang, Y.; Yang, J.; Cao, X. H.; Lu, Q. P.; Zhang, X.; Z. Zhang, Z. C.; Tan, C. L.; Zhang, H. Synthesis of Two-Dimensional $CoS_{1.097}$/Nitrogen-Doped Carbon Nanocomposites using Metal-Organic Framework Nanosheets as Precursors for Supercapacitor Application, *J. Am. Chem. Soc*. **2016**, 138 (22), 22, 6924–6927.

45 Huang, Y.; Wang, J. Z.; Ma, S. L.; Wang, R. A Confined MoN_2@N-Rich Carbon Catalyst Derived from β-Cyclodextrin Encapsulating Phosphomolybdic Acid for Oxidative Removal of H_2S. *Chem. Eng. J.* **2023**, 457, 141389.

46 Kafle, A.; M Kumar, M.; D Gupta, D.; Nagaiah, T. C. The Activation-Free Electroless Deposition of NiFe over Carbon Cloth as a Self-Standing Flexible Electrode towards Overall Water Splitting. *J. Mater. Chem. A*, **2021**, 9, 24299-24307.

47 Yu, L.; Song, S. W.; McElhenny, B.; Ding, F. Z.; Luo, D.; Yu, Y.; Chen, S.; Ren, Z. F. A Universal Synthesis Strategy to Make Metal Nitride Electrocatalysts for Hydrogen Evolution Reaction. *J. Mater. Chem. A*, **2019**, 7, 19728-19732.

48 McCue, A. J.; Anderson, J. A. Recent Advances in Selective Acetylene Hydrogenation Using Palladium Containing Catalysts. *Front. Chem. Sci. Eng*. **2015**, 9, 142-153.

49 Trimm, D. L.; Liu I. O. Y.; Cant. N. W. The Oligomerization of Acetylene in Hydrogen over Ni/SiO_2 Catalysts: Product Distribution and Pathways. *J. Mol. Cata. A Chem.* **2008**, 288, 63-74.

50 Bridier, B.; López, N.; Pérez-Ramírez, J. Partial Hydrogenation of Propyne over Copper-Based Catalysts and Comparison with Nickel-Based Analogues. *J. Catal*. **2010**, 269 (1), 80-92.

51 Okamoto, H. Ni-S (Nickel-Sulfur). *J. Phase Equilib. Diffus*. **2009**, 30, 123.

52 Ma, H. Y.; Wang, G. Selective Hydrogenation of Acetylene on Pt_n/TiO_2 (n = 1, 2, 4, 8) Surfaces: Structure Sensitivity Analysis. *ACS Catal.* **2020**, 10, 4922-4928.

53 Xia, Z. H.; Guo, S. J. Strain Engineering of Metal-Based Nanomaterials for Energy Electrocatalysis. *Chem. Soc. Rev*. **2019**, 48, 3265.

54 Hu, N. M.; Yang, C. H.; He, L.; Guan, Q. Q.; Miao, R. R. Ni–Cu/Al_2O_3 Catalysts for the Selective Hydrogenation of Acetylene: A Study on Catalytic Performance and Reaction Mechanism. *New J. Chem*. **2019**, 43, 18120-18125.

55 Mei, D. H.; Neurock, M.; Smith, C. M. Hydrogenation of Acetylene–Ethylene Mixtures over Pd and Pd–Ag Alloys: First-Principles-Based Kinetic Monte Carlo Simulations. *J. Catal*. **2009**, 268 (2), 181-195.

56 Sheth, P. A.; Neurock, M.; Smith, C. M. First-Principles Analysis of the Effects of Alloying Pd with Ag for the Catalytic Hydrogenation of Acetylene-Ethylene Mixtures. *J. Phys. Chem. B* **2005**, 109 (25), 12449–12466.

57 Song, Y.; Laursen, S. Control of Surface Reactivity towards Unsaturated CAC Bonds and H over Ni-based Intermetallic Compounds in Semi-hydrogenation of Acetylene. *J. Catal.* **2019**, 372, 151–162.

Graphical abstract

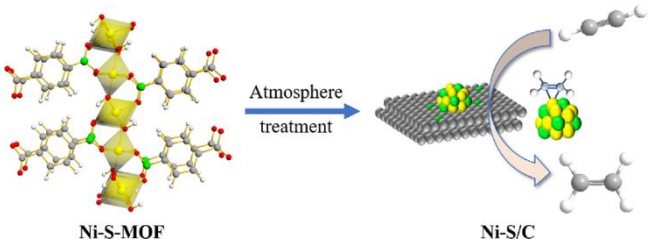

Supporting Information

Metal organic framework derived Ni-S/C catalysts for selective alkyne hydrogenation

Ning Li,[1,2,δ] Shaoxia Weng,[1,2,δ] Alan J. McCue,[3] Yuanfei Song,[1,2] Yufei He,[1,2] Yanan Liu,[1, 2,*] Junting Feng,[1,2] Dianqing Li[1, 2, *]

[1]*State Key Laboratory of Chemical Resource Engineering, Beijing Engineering Center for Hierarchical Catalysts, Beijing University of Chemical Technology, Beijing, 100029, China*

[2] *Quzhou Institute for Innovation in Resource Chemical Engineering, Quzhou, 324000, China*

[3] *Department of Chemistry, University of Aberdeen, Aberdeen AB24 3UE, U.K.*

* Corresponding author

Address: Box 98, 15 Bei San Huan East Road, Beijing 100029, China

Tel: +86 10 64436992 Fax: +86 10 64436992

E-mail: ynliu@mail.buct.edu.cn (Yanan Liu); lidq@mail.buct.edu.cn (Dianqing Li)

[δ] These two authors contribute equally

1. EXPERIMENTAL DETAIL

1.1. Chemical materials

$Ni(NO_3)_2 \cdot 6H_2O$ was bought from Aladdin. N, N-Dimethylformamide (DMF) and terephthalic acid were purchased from Macleans. Dimethyl sulfoxide (DMSO) and thiourea were bought Sigma-Aldrich. Anhydrous methanol and anhydrous ethanol were purchased from Tianjin damao chemical reagent factory. All chemicals were of analytical grade. Deionized water with conductivity less than 10^{-6} S/cm was used.

1.2. Synthesis of contrast catalysts

For comparison, Ni-S-MOF was also treated at 600 ℃ and 800 ℃ while other preparation conditions remain unchanged to obtain Ni-S/C-600 and Ni-S/C-800. Ni_3S_2/Al_2O_3 was synthesized by a traditional impregnation approach [1]. Specifically, 0.52 g of $Ni(NO_3)_2 \cdot 6H_2O$ and 0.85 g of thiourea were dissolved in 10 mL of deionized water. Then, 1.00 g of γ-Al_2O_3 was added into the solution which was stirred for 2 h at 60 ℃ before being dried at 60 ℃ for 12 h. The resulting solid was then treated at 300 ℃ for 2 h in a 10 vol% H_2/N_2 with flow rate of 55 mL/min to obtain a Ni_3S_2/Al_2O_3 catalyst. Similarly, a Ni/Al_2O_3 catalyst was also prepared using the same procedure but without addition of thiourea.

1.3. Catalyst testing

The reactant and product concentrations were analyzed by online gas chromatography (GC) with a flame ionization detector using a PLOT capillary column (50 m × 0.53 mm). Propane was used as an internal standard. Multiple data points were collected for a given set of conditions (i.e., different temperatures) to ensure data reproducibility. Acetylene conversion, TOF, ethylene, ethane and oligomer of selectivity were calculated as following:

$$Acetylene\ conversion = \frac{acetylene(inlet) - acetylene(outlet)}{acetylene(inlet)}$$

$$Ethylene\ selectivity = \frac{ethylene(outlet) - ethylene(inlet)}{acetylene(inlet) - acetylene(outlet)}$$

$$Ethane\ selectivity = \frac{ethane(outlet) - ethane(inlet)}{acetylene(inlet) - acetylene(outlet)}$$

$$Oligomer\ selectivity = 1 - ethylene\ selectivity - ethane\ selectivity$$

$$TOF = \frac{C \times L \times M \times 10^{-3}}{V_m \times m \times w \times D \times 60}$$

where C is conversion of acetylene (%); L is the flow rate of acetylene (mL min^{-1}); V_m is molar volume of gas (L mol^{-1}); M stands for atomic mass of Ni; m is quality of catalyst (g); w is the metal loading (wt. %); D is metal dispersion (%).

1.4. Catalyst characterization

Powder X-ray Diffraction (XRD) data was acquired in the range of 2θ = 5-60° using Cu K_a radiation (λ=0.154 nm) using a Shimadzu XRD-6000 instrument. The elemental content of the active metals was determined using a Shimadzu ICPS-7500 Inductively Coupled Plasma Atomic Emission Spectrometer (ICP-AES). Raman analysis was performed using a HORIBA Jobin Yvon HR800 Raman spectrometer and a 532 nm argon ion laser as excitation source. The FTIR spectra were obtained on a Bruker Tensor 27 instrument with a highly sensitive MCT detector and a diffuse reflectance IR heating chamber with a KBr window. A JEOL JEM-2100F electron microscope with Energy Dispersive X-ray (EDX) mapping was used to determine the size and elemental distribution of samples. X-ray Photoelectron Spectroscopy (XPS) characterization was performed on an ESCALAB 250 spectrometer with Al Kα radiation using the C 1s peak at 284.6 eV as reference. Temperature programmed experiments were conducted using a Micrometric ChemiSorb instrument (Micrometric ChemiSorb 2750) with a TCD detector. 0.1 g of sample was placed in the center of a quartz tube and pretreated at 120 °C for 1 h in Ar for to clean the catalyst surface followed by cooled to room temperature. For a H_2-TPD experiment, H_2 was passed through for adsorption until saturation before the sample holder was purged with Ar for 1 h to remove any physically adsorbed hydrogen. Then, desorption signal was recorded as the sample temperature was increased from 50 to 250 °C at a heating rate of 10 °C /min. For C_2H_4-TPD, the same procedure was used with the exception that the purge gas was changed to He, and then

sample was heated in the range of 50-340 ºC for desorption. H_2 pulse chemisorption was performed on a Micromeritics Autochem II 2920 instrument. After pre-treatment, the chemisorption was carried out by pulsing of a mixture of 10% H_2/Ar (30 mL min^{-1}). The dispersion of active nickel was calculated from the volume of H_2 adsorbed by assuming the stoichiometry of $H_{adsorbed}/Ni_{surface}$ being 1. The pyrolysis temperature of the samples was analyzed in a nitrogen and air stream using a TG/DTA X70 Thermogravimetric Analyzer (NETZSCH). FTIR spectra of adsorbed CO were obtained using a Bruker Tensor 27 instrument with a crystal quartz reaction cell with a KBr window, and in transmission mode. The sample powder was pre-treated in H_2/Ar at 300 °C for 2 h, followed by purging in Ar. After cooling to 30 °C in Ar, the background spectra were recorded. The spectra of adsorbed CO were recorded after introducing 99.99% CO into the reactor for 0.5 h and purging Ar for a further 1 h to remove any gas-phase CO. In situ Diffuse Reflectance Infrared Fourier Transform Spectroscopy (DRIFTS) reactions were performed using a Bruker Tensor II instrument. The catalysts were first pretreated with 10.0 vol% H_2/N_2 at 300 ºC for 2 h, before a background spectrum was collected at a resolution of 4 cm^{-1}. After cooling to 25 °C under an Ar flow, C_3H_4/N_2 were introduced and the sample temperature increased incrementally to 160°C.

1.5. DFT calculation

All the first-principles spin-polarized calculations were performed by using the Vienna ab initio Simulation Program (VASP). The generalized gradient approximation (GGA) in the Perdew-Burke-Ernzerhof (PBE) form and a cutoff energy of 500 eV for planewave basis set were adopted. A 5 × 5 × 1 Monkhorst-Pack k grid was used for sampling the Brillouin zones at structure calculation. The ion-electron interactions were described by the projector augmented wave (PAW) method. The convergence criteria of structure optimization were selected as the maximum force on each atom less than 0.01 eV/Å with an energy change less than 1×10^{-5} eV. To calculate the kinetic energy barrier of chemical reactions, the climbing image nudged elastic band (CI-NEB) method was used to search for the transition states.

2. ADDITIONAL RESULTS

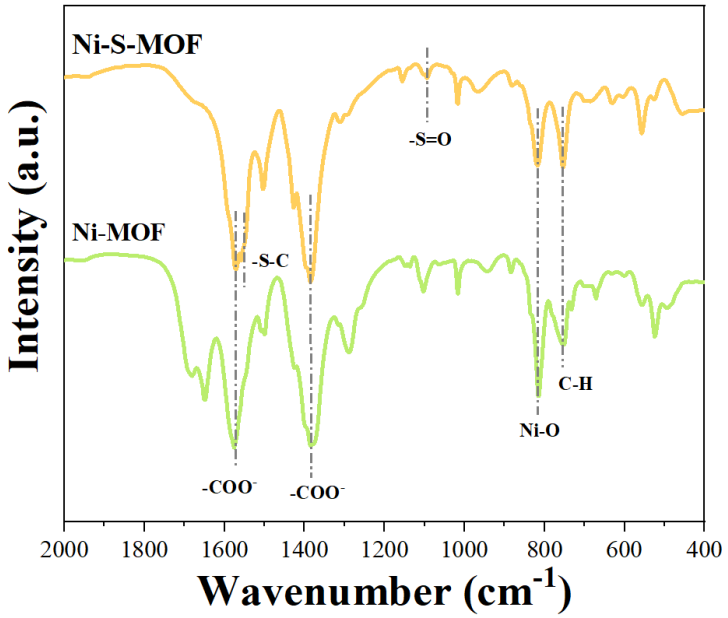

Figure S1 FTIR spectra of MOF precursors

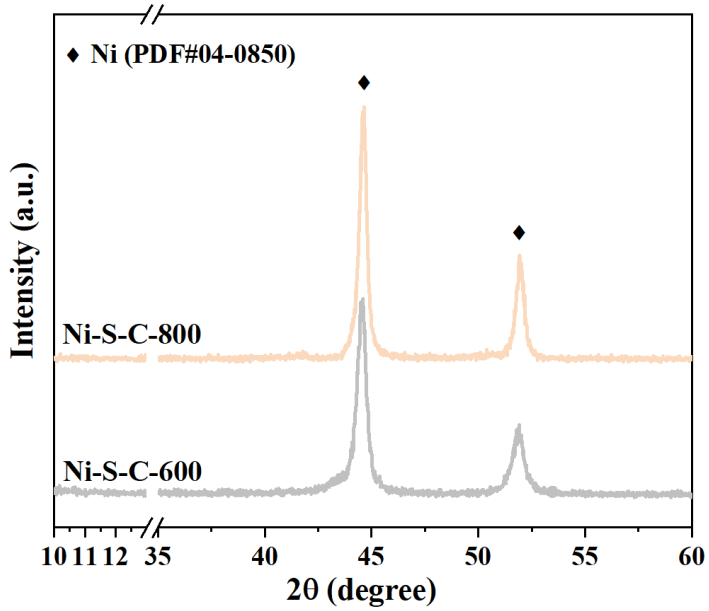

Figure S2 XRD patterns of Ni-based catalysts derived at 600 °C and 800 °C

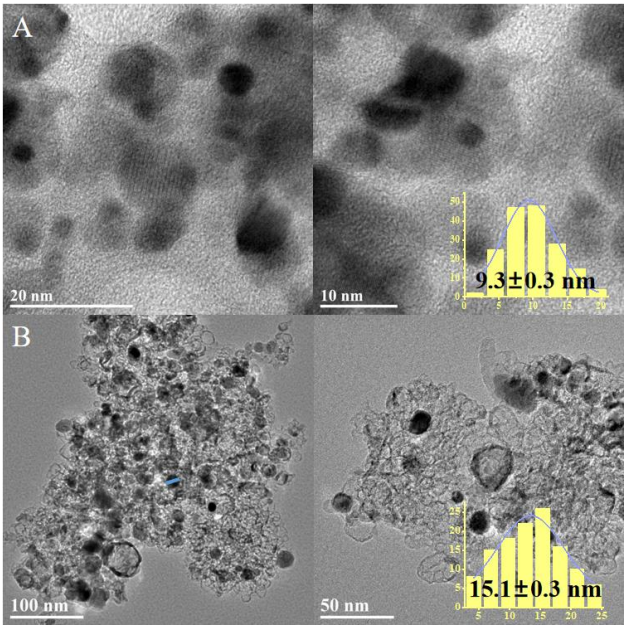

Figure S3 HRTEM images and particle sizes of Ni-S/C derived at (A) 600 ºC (B) 800 ºC

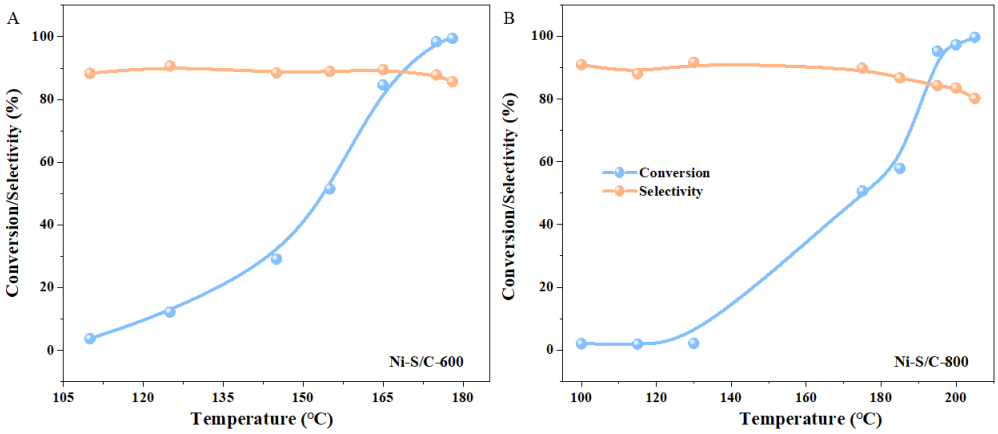

Figure S4 Catalytic performance of Ni-S/C derived at (A) 600 ºC (B) 800 ºC

The diffraction patterns of the underlying MOF structure treated at 300 ºC, 600 ºC and 800 ºC are all lost suggesting the structure collapse of MOF even though at lower temperature. More importantly, relative to Ni-S/C-600 and Ni-S/C-800, Ni-S/C treated at 300 ºC exhibits the highest catalytic activity and selectivity due to the aggregation of active Ni particles (9-15 nm) and loss of S element (ca. 0.5%) at the elevated temperatures. Overall, 300 ºC is selected for pyrolysis in our situation.

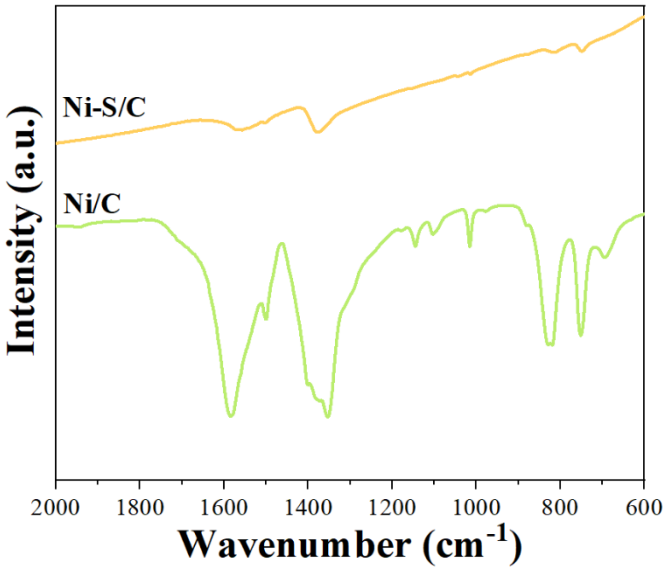

Figure S5 FTIR spectra of Ni-based catalysts derived from MOF precursors

Table S1 Properties of MOF derived catalysts

Catalysts	Ni-S/C	Ni/C
d_{VA} (nm)	7.7	10.0
Dispersion (%)	16.8	11.6

Table S2 Ni K-edge EXAFS parameters fitted for the samples

Samples	Scattering pair	CN[a]	r[b] (Å)	ΔE[c] (eV)	σ^{2d}	R factor
Ni-S/C	Ni-Ni	5.1	2.50	-7.8	0.009	0.009
	Ni-S	3.2	2.21	1.6	0.008	

[a] Coordination number (CN) [b] Atomic distance (r)

[c] Energy difference in the absorption threshold between the reference and the target samples (ΔE)

[d] Debye-Waller factor (σ^2)

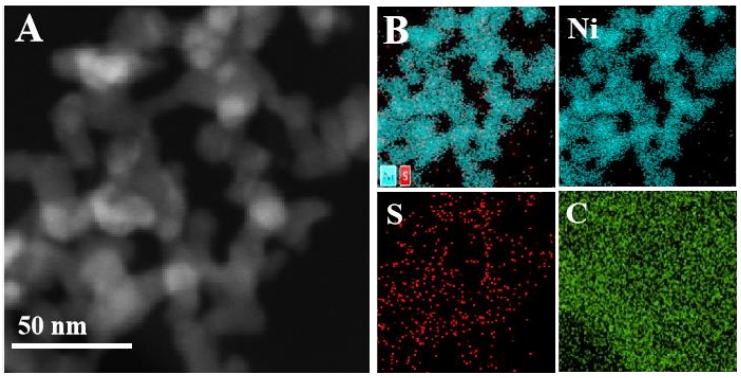

Figure S6 The corresponding EDX elemental mappings of Ni-S/C catalysts

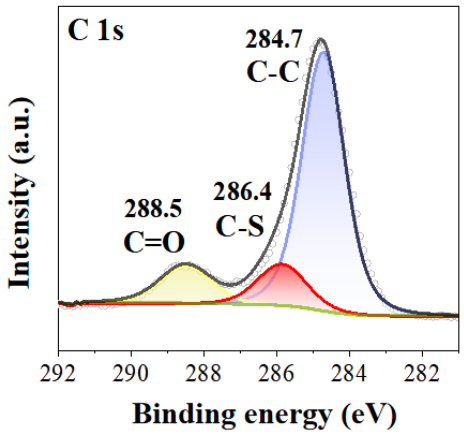

Figure S7 High-resolution C 1s XP spectra of Ni catalysts

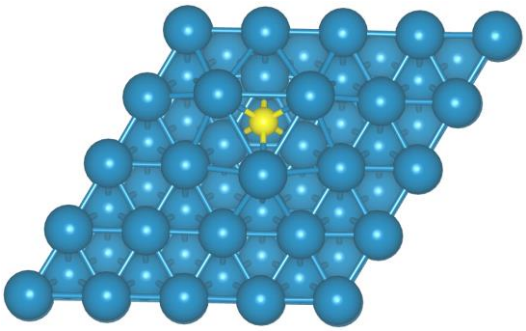

Figure S8 Density functional theory (DFT) calculations of top view of optimized configurations of S-modified Ni (111).

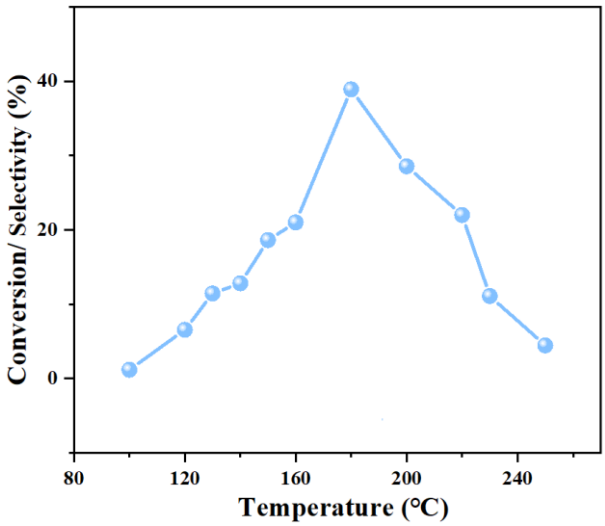

Figure S9 Catalytic performance of Ni/C derived at 600 °C

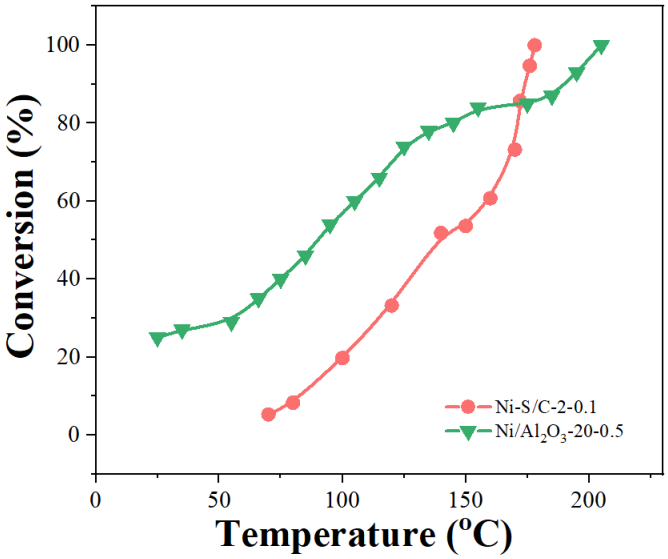

Figure S10 Acetylene conversion as a function of temperature for Ni-S/C and a reference Ni/Al_2O_3. Reaction conditions: 0.1 g Ni-S/C (SV = 13200 h^{-1}) or 0.5 g Ni/Al_2O_3 (18700 h^{-1}), 2:1 H_2/C_2H_2 ratio for Ni-S/C and 20:1 for Ni/Al_2O_3, total flow = 218 mL min^{-1}, temperature in range of 25-210 °C.

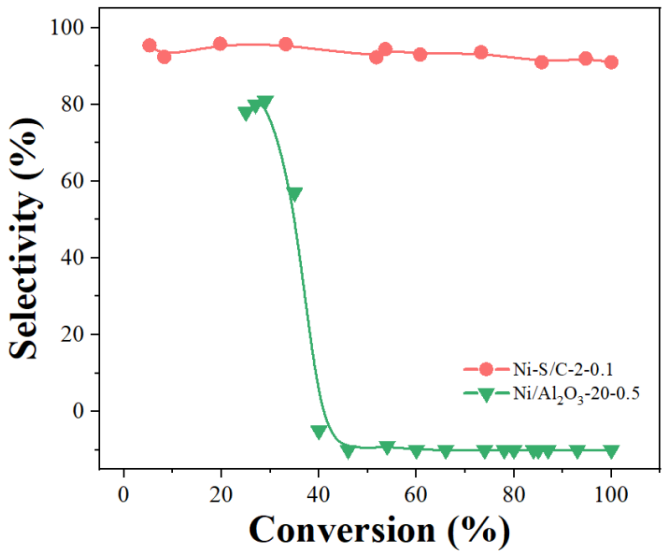

Figure S11 Ethylene selectivity as a function of acetylene conversion for Ni-S/C and a reference Ni/Al_2O_3. Reaction conditions: 0.1 g Ni-S/C (SV = 13200 h^{-1}) or 0.5 g Ni/Al_2O_3 (18700 h^{-1}), 2:1 H_2/C_2H_2 ratio for Ni-S/C and 20:1 for Ni/Al_2O_3, total flow = 218 mL min^{-1}, temperature in the range of 25-210 °C.

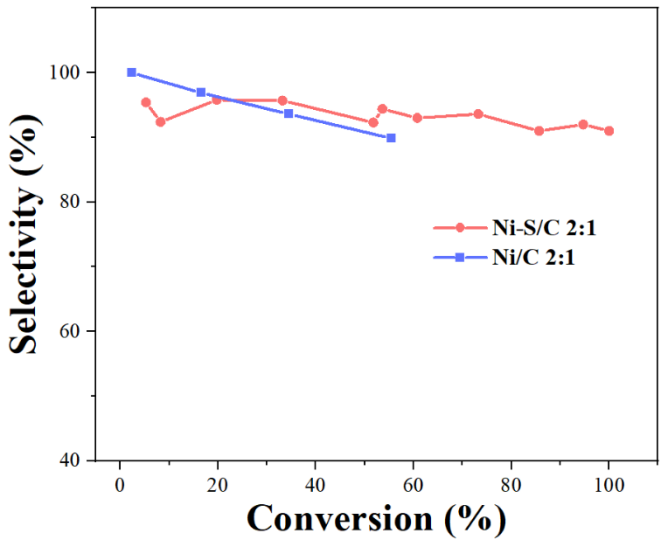

Figure S12 Ethylene selectivity as a function of acetylene conversion over Ni-based catalysts

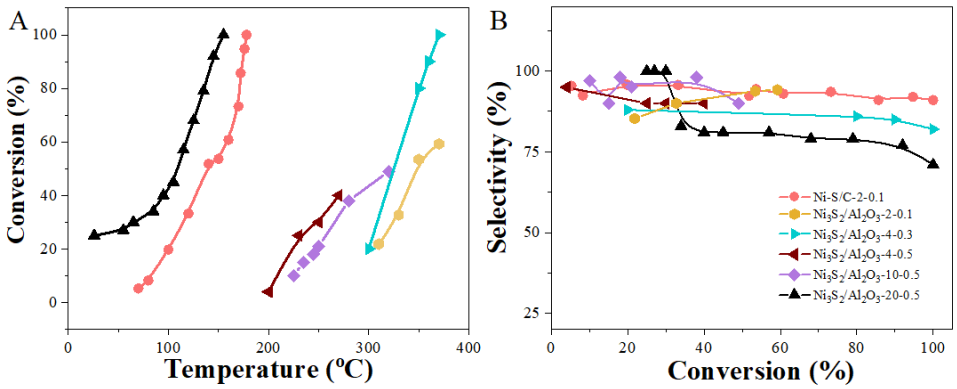

Figure S13 (A) Acetylene conversion as a function of temperature; (B) Selectivity of ethylene as a function of acetylene conversion over the reference Ni_3S_2/Al_2O_3 catalyst. Reaction conditions: 0.1-0.5 g in sample coding refers to catalyst mass used, 2-20 in the sample coding refers to H_2/C_2H_2 ratio, total flow = 218 mL min^{-1}, SV = 43600 h^{-1} for 0.1 g catalysts, SV = 26160 h^{-1} for 0.3 g catalysts, SV = 18700 h^{-1} for 0.5 g catalysts, temperature in the range of 25-350 °C.

Table S3 Catalytic performance of Ni-based catalysts by changing the reaction conditions

Catalysts	Amount (g)	Reaction temperature (°C)	H_2/C_2H_2	Conv. (%)	Sel. (%)
Ni-S/C	0.1	25-178	2:1	100	90.9
Ni/Al_2O_3	0.5	70-190	20:1	100	<0
Ni_3S_2/Al_2O_3	0.1	310-370	2:1	58.5	94.8
Ni_3S_2/Al_2O_3	0.3	300-370	4:1	100	82.5
Ni_3S_2/Al_2O_3	0.5	180-270	4:1	40.5	90.2
Ni_3S_2/Al_2O_3	0.5	225-320	10:1	48.9	90.4
Ni_3S_2/Al_2O_3	0.5	25-155	20:1	100	71.0

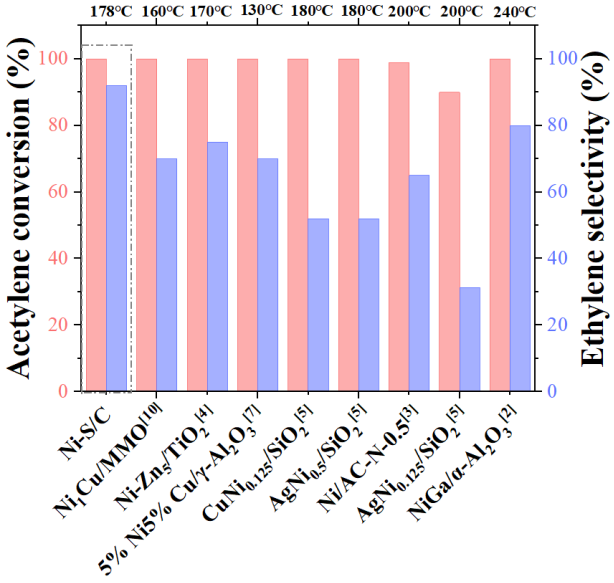

Figure S14 Comparison of catalytic performance with Ni-based catalysts reported in literature

Table S4 Comparison of catalytic performance with Ni-based catalysts reported in literature

Catalysts	T (°C)	H_2/C_2H_2	SV (h^{-1})	Con. (%)	Sel. (%)	Ea (kJ/mol)
Ni-S/C	178	2:1	13200	100	92	28.2
NiGa/α-Al_2O_3[2]	240	20:1	4800	100	80	-
Ni/AC-N-0.5[3]	200	3:1	4000	99	65	-
Ni–Zn_5/TiO_2[4]	170	10:1	20000	100	75	-
$CuNi_{0.125}/SiO_2$[5]	140	20:1	60000	100	40	54.5
$AgNi_{0.5}/SiO_2$[5]	180	20:1	60000	100	62	52.8
$AuNi_{0.5}/SiO_2$-H_2-450[6]	300	20:1	60000	100	70	-
5%Ni5%Cu/γ-Al_2O_3[7]	130	2:1	-	100	70	-
Ni@CeO_2[8]	200	3.85:1	-	70	-	42.7
NiCu/MMO[9]	160	2:1	8040	100	70	34.2
Ni_4Ga/SiO_2[10]	180	5:1	36000	100	78	-
Pre-Al-Ni/MMO[11]	140	2:1	8040	100	78	34.3
Si-Ni-Zn[12]	200	10:1	128000	97	80	26.6

Mass and Heat Transfer Calculations for acetylene hydrogenation on Ni-S/C catalyst. (0.45C_2H_2/0.91H_2/45.00C_2H_4/1.00 C_3H_8/N_2, T=451 K，acetylene conversion ~100%)

Mears Criterion for External Diffusion (Fogler, p841; Mears, 1971)

If $\frac{-r_A'\rho_b Rn}{k_c C_{Ab}} < 0.15$, then external mass transfer effects can be neglected.

$-r_A'$ = reaction rate, kmol/kg·cat·s

n = reaction order

R = catalyst particle radius, m

ρ_b = bulk density of catalyst bed, kg/m^3

ρ_c = solid catalyst density, kg/m^3

C_{Ab} = bulk gas concentration of A, kmol/m^3

k_c = mass transfer coefficient, m/s

Sherwood number (Sh) = $k_c(2R_p)/D_{AB}$

$Sh = 2+0.6Re^{1/2}Sc^{1/3}$

Reynolds number (Re) = $2U\cdot R\cdot\rho/\mu$ (where U is superficial velocity in m/s, ρ is the density of the reactant mixture fluid, estimated using C_2H_2/N_2 at 451K, μ is the viscosity of the reactant mixture fluid, estimated using C_2H_2/N_2 at 451K)

Schmidt number (Sc) = $\mu/\rho\cdot D_{AB}$

$D_{AB} = 18.583T^{1.5}[(M_1+M_2)/M_1M_2]^{0.5}/P\cdot\sigma_{12}^2\Omega$ (where D_{AB} is gas-phase diffusivity in m^2/s, T is temperature in K, M is the molecular mass in kg/kmol, P is the pressure in bar, Ω is collision integral, σ_{12} is constant of Lennard-Jones potential energy function.

$\frac{-r_A'\rho_b Rn}{k_c C_{Ab}}$ = [1.90×10^{-7} kmol/kg·s] [1272.72 kg/m^3] [3.85 × 10^{-9}m] [0.1] / ([3.94 m/s] [6.65×10^{-4} kmol/m^3]) = 3.55×10^{-11}<0.15 {Mears for External Diffusion}

Weisz-Prater Criterion for Internal Diffusion (Fogler, p839)

If $C_{WP} = \frac{-r'_{A(obs)}\rho_c R^2}{D_e C_{As}} < 1$, then internal mass transfer effects can be neglected.

-r'$_{A(obs)}$ = observed reaction rate, kmol/kg·cat·s

R = catalyst particle radius, m

ρ_c = solid catalyst density, kg/m^3;

D_e = effective gas-phase diffusivity, m^2/s **[Fogler, p815]**

$$= \frac{D_{AB}\phi_p\sigma_c}{\tau} \quad \text{where}$$

D_{AB} = gas-phase diffusivity m^2/s; ϕ_p = pellet porosity; σ_c =constriction factor; τ =tortuosity.

C_{As} = gas concentration of A at the catalyst surface, kmol-A/m^3

$$C_{WP} = \frac{-r'_{A(obs)}\rho_c R^2}{D_e C_{As}} = [1.90\times10^{-7} \text{ kmol/kg·s}]\ [97.67 \text{ kg/m}^3]\ [3.85\times10^{-9} \text{ m}]^2 / ([8.36\times10^{-9} \text{ m}^2/\text{s}]$$

$[6.65\times10^{-4} \text{ kmol/m}^3]) = \mathbf{4.95\times10^{-10} < 1}$

{Weisz-Prater Criterion for Internal Diffusion}

Mears Criterion for External (Interphase) Heat Transfer (Fogler, p842)

$$\left|\frac{-\Delta H_r(-r_A')\rho_b RE}{h_t T_b^{\,2} R_g}\right| < 0.15$$

Nusselt number (Nu) = $2 + 0.6Re^{1/2}Sc^{1/3}$

$Nu = h_t(2R_p)/\lambda$

$[176 \text{ kJ/mol} \times 1.90\times10^{-4} \text{ mol/kg·s} \times 1272.72 \text{ kg/m}^3 \times 3.85 \times 10^{-9} \text{ m} \times 28.2 \text{ kJ/mol}] / [22.4 \text{ kJ/m}^2\text{·K·s} \times 451^2 \text{ K}^2 \times 8.314 \times10^{-3} \text{ kJ/mol·K}] = 1.20\times10^{-10} < 0.15$

{Mears Criterion for External (Interphase) Heat Transfer}

Mears Criterion for Combined Interphase and Intraparticle Heat and Mass Transport (Mears, 1971)

$$\frac{-r'_A R^2}{C_{Ab} D_e} < \frac{1+0.33\gamma\chi}{|n-\gamma_b\beta_b|(1+0.33n\omega)}$$

$$\gamma = \frac{E}{R_g T_s};\quad \gamma_b = \frac{E}{R_g T_b};\quad \beta_b = \frac{(-\Delta H_r) D_e C_{Ab}}{\lambda T_b};\quad \chi = \frac{(-\Delta H_r) - r'_A R}{h_t T_b};\quad \omega = \frac{-r'_A R}{k_c C_{Ab}}$$

γ = Arrhenius number; β_b = heat generation function;

λ = catalyst thermal conductivity, W/m·K;

χ = Damköhler number for interphase heat transport

ω = Damköhler number for interphase mass transport

$$\frac{-r'_A R^2}{C_{Ab} D_e} = [1.90\times10^{-7} \text{ kmol/kg·s} \times (3.85\times10^{-9})^2 \text{ m}^2]/[\ 6.65 \times 10^{-4} \text{ kmol/m}^3 \times 8.36\times10^{-9} \text{ m}^2/\text{s}] = 1.32\times$$

$10^{-13} < 1.67$

{Mears Criterion for Interphase and Intraparticle Heat and Mass Transport}

Table S5 Parameters used in the Mears criterion and Weisz-Prater Criterion for estimating mass and heat transfer limitations in semi-hydrogenation of acetylene

Parameters	Value
Reaction rate at 451 K:-r_A(kmol/kg_{cat} s)	~1.90×10^{-7}
Density of catalyst: ρ_c(Kg/m^3)	~97.67
Catalyst bed density: ρ_b(Kg/m^3)	~1272.72
Radius of catalyst: R(m)	~3.85×10^{-9}
Radius of quartz tube: r(m)	~3.50×10^{-3}
Reaction order: $n_{(C2H2)}$	~ 0.1
Bulk gas concentration of C_2H_2 at 451 K: C_{Ab} (kmol/m^3)	~6.65×10^{-4}
Viscosity of the reactant at 451 K: (μC_2H_4)/ (μN_2)(Pa·s)	~1.26×10^{-5}/2.10×10^{-5}
Viscosity of the reactant mixture fluid at 451 K: μ (Pa·s)[a]	~1.47×10^{-5}
Density of reactant mixture fluid at 451 K:ρ (Kg/m^3)[b]	~0.94
Re	~1.39×10^{-2}
Sc	~2.78
Sh	~2.10
Gas-phase diffusivity: D_{AB} (m^2/s)	~5.63×10^{-6}
Mass transfer coefficient: k_c (m/s)	~3.94
Effective gas-phase diffusivity: D_e (m^2/s)	~8.36×10^{-9}
Heat of reaction: ΔHr (kJ/mol)	~176
Activation energy: E (kJ/mol)	~28.2
Thermal conductivity at 451 K: λC_2H_4/λN_2 (W/m·K)	~3.23×10^{-2}/3.15×10^{-2}
Thermal conductivity of reactant mixture fluid at 451 K: λ (W/m·K)[c]	~3.20×10^{-2}
Nu	~2.10
Heat transfer coefficient: h_t (W/m^2·K)	~2.24×10^4

[a] estimated based on Wilke formula

[b] estimated based on gas component

[c] estimated based on Wassiljewa calculation

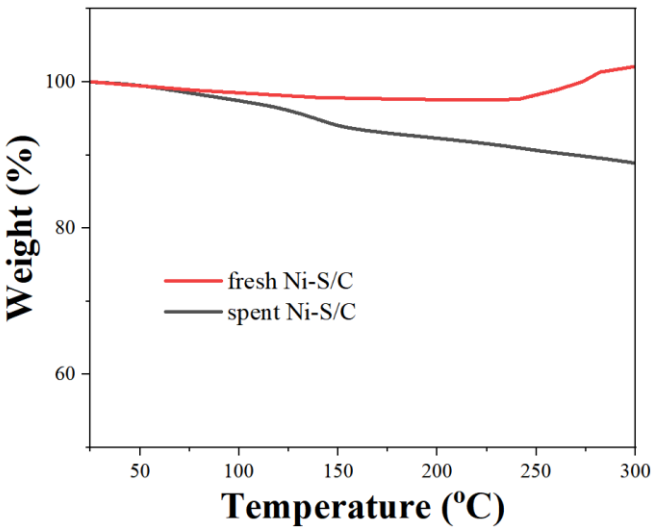

Figure S15 TG profiles of fresh and spent Ni-S/C catalyst (The unusual weight increase for fresh Ni-S/C catalyst may be attributed to the partial oxidation of metal particles[15])

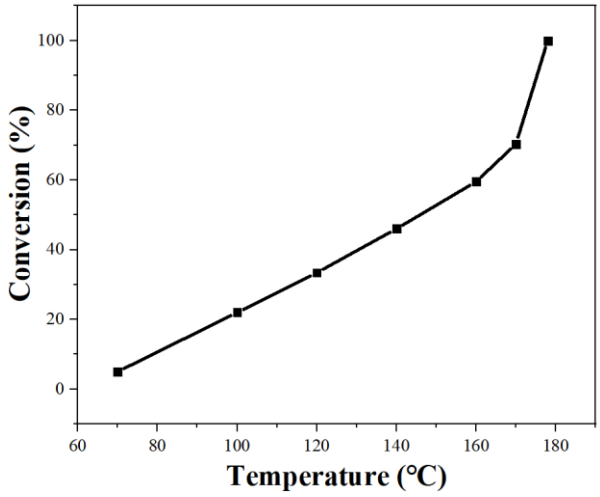

Figure S16 The activity of spent Ni-S/C sample after coke was removed

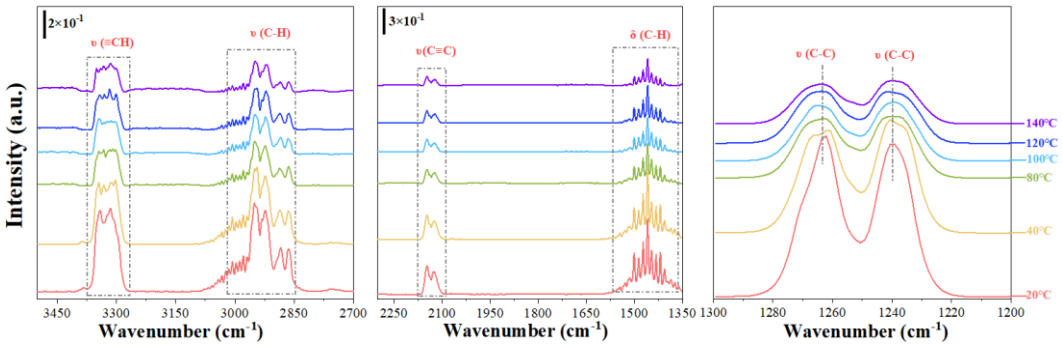

Figure S17 In situ DRIFT spectra of adsorbed alkyne in Ni-S/C catalyst

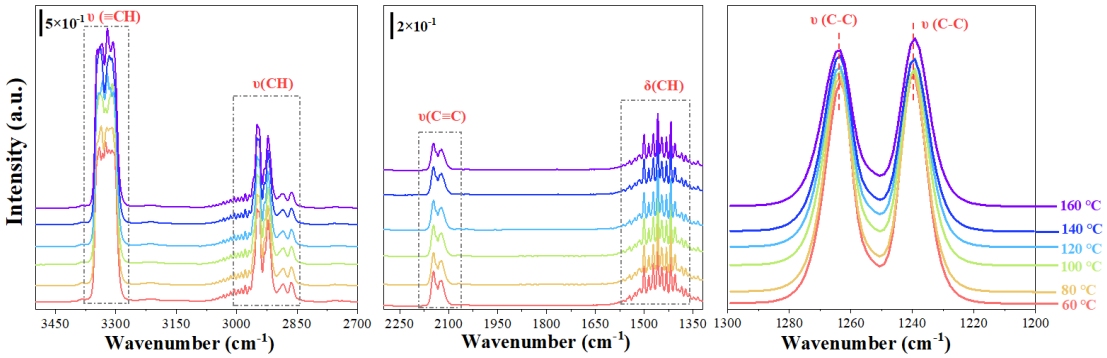

Figure S18 In situ DRIFT spectra of adsorbed alkyne on Ni/C catalyst

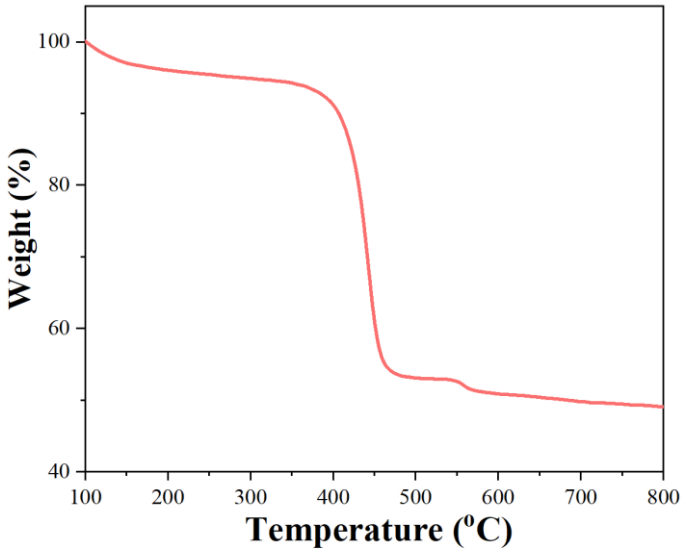

Figure S19 N_2-TG analysis of fresh Ni-S/C catalyst

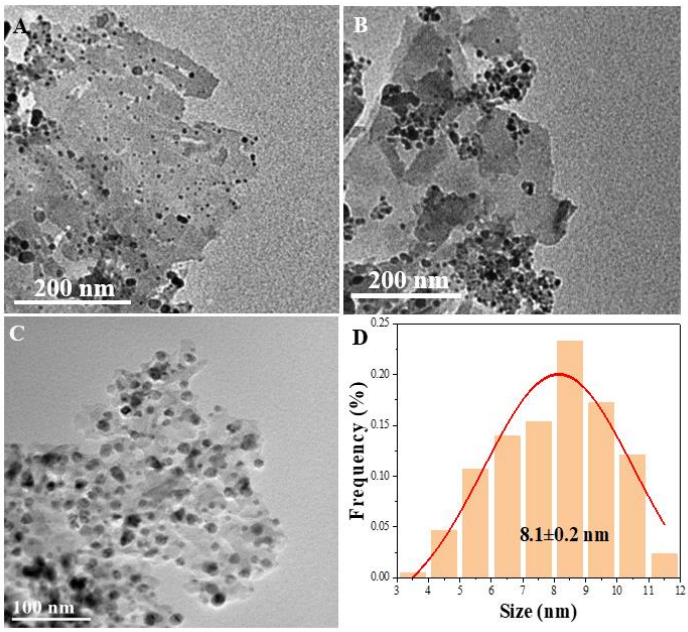

Figure S20 HRTEM images of spent Ni-S/C catalyst

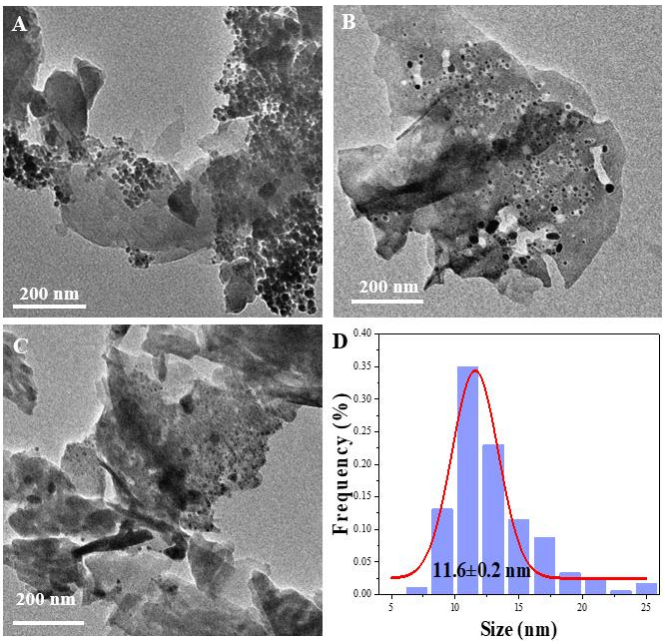

Figure S21 HRTEM images of spent Ni/C catalyst

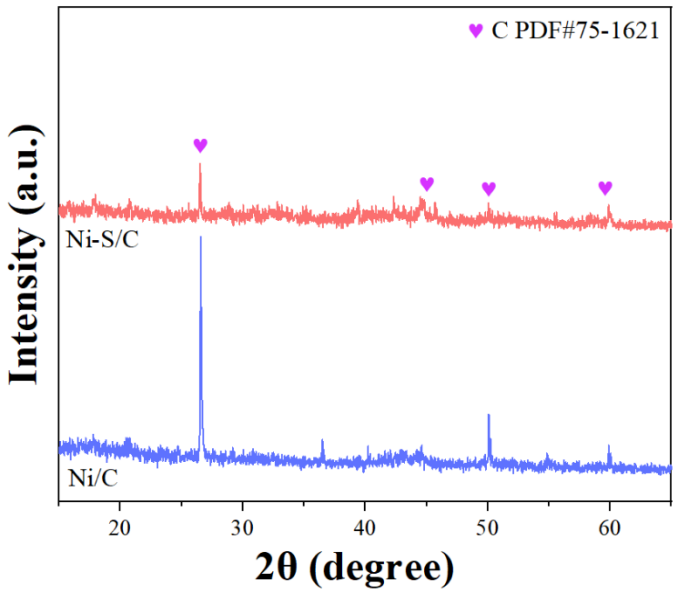

Figure S22 XRD patterns of spent Ni-S/C and Ni/C catalysts

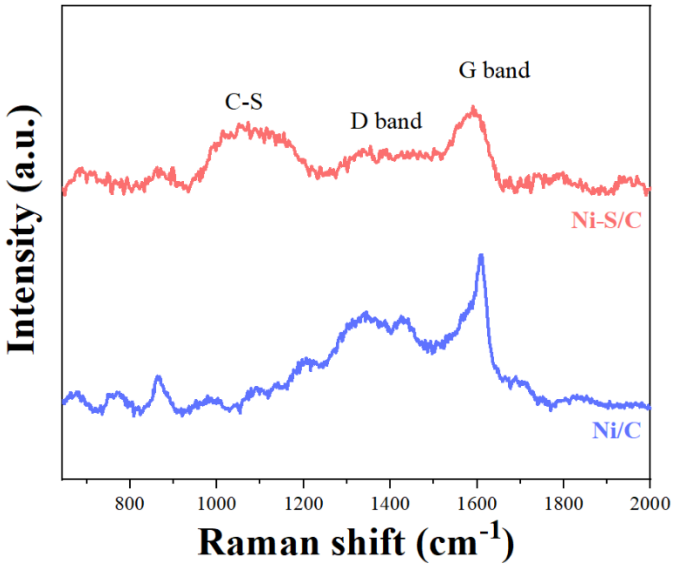

Figure S23 Raman spectra of spent Ni-S/C and Ni/C catalysts

Reference

1. Fu, B. A.; McCue, A. J.; Liu, Y. N.; Weng, S. X.; Song, Y. F.; He, Y. F.; Feng, J. T.; Li, D. Q. Highly Selective and Stable Isolated Non-Noble Metal Atom Catalysts for Selective Hydrogenation of Acetylene. *ACS Catal*. **2022**, 12 (1), 607-615.
2. Li, Q. Y.; Wang, Y. X.; Skoptsov, G.; Hu, J. L. Selective Hydrogenation of Acetylene to Ethylene over Bimetallic Catalysts. *Ind. Eng. Chem. Res*. **2019**, 58 (45), 20620–20629.
3. Xu, Z.; Zhou, S. Z.; Zhu, M. Y. Ni Catalyst Supported on Nitrogen-Doped Activated Carbon for Selective Hydrogenation of Acetylene with High Concentration. *Catal. Commun*. **2021**, 149 (15), 106241.
4. Wang, Z.; Wang, G.; Louis, C.; Delannoy, L. Bimetallic Ni–Zn/TiO_2 Catalysts for Selective Hydrogenation of Alkyne and Alkadiene Impurities from Alkenes Stream. *Res. Chem. Intermed*. **2021**, 47, 91–116.
5. Liu, H.; Chai, M. Q.; Pei, G. X.; Liu, X. Y.; Li, L.; Kang, L. L.; Wang, A. Q.; Tao Zhang, T. Effect of IB-Metal on Ni/SiO_2 Catalyst for Selective Hydrogenation of Acetylene. *Chinese J. Catal*. **2020**, 41 (7), 1099-1108.
6. Pei, G. X.; Liu, X. Y.; Wang, A. Q.; Su, Y.; Li, L.; Zhang, T. Selective Hydrogenation of Acetylene in an Ethylene-Rich Stream over Silica Supported Ag-Ni Bimetallic Catalysts. *Appl. Catal. A Gen*. **2017**, 545, 90-96.
7. Hu, N. M.; Yang, C. H.; He, L.; Guan, Q. Q.; Miao, R. R. Ni–Cu/Al_2O_3 Catalysts for the Selective Hydrogenation of Acetylene: a Study on Catalytic Performance and Reaction Mechanism. *New J. Chem*. **2019**, 43, 18120-18125.
8. Riley, C.; Zhou, S. L.; Kunwar, D.; Riva, A. D. L.; Peterson, E.; Payne, R.; Gao, L. Y.; Lin, S.; Guo, H.; Datye, A. Design of Effective Catalysts for Selective Alkyne Hydrogenation by Doping of Ceria with a Single-Atom Promotor. *J. Am. Chem. Soc*. **2018**, 140 (40), 12964–12973.
9. Liu, Y. N.; Zhao, J. Y.; Feng, J. T.; He, Y. F.; Du, Y. Y.; Li, D. Q. Layered Double Hydroxide-Derived Ni-Cu Nanoalloy Catalysts for Semihydrogenation of Alkynes: Improvement of Selectivity and Anti-Coking Ability via Alloying of Ni and Cu. *J. Catal*. **2018**, 359, 251-260.
10. Wang, L.; Li, F. X.; Chen, Y. J.; Chen, J. X. Selective Hydrogenation of Acetylene on SiO_2-Supported Ni-Ga Alloy and Intermetallic Compound. *J. Energy Chem*. **2019**, 29, 40-49.

11. Yuan, Z. J.; Kumar, A.; Zhou, D. J.; Feng, J. T.; Liu, B.; Sun, X. M. Highly Efficient Semi-Hydrogenation of Acetylene over Ni Supported Mesoporous $MgAl_2O_4$ Spinel Derived from Aluminate-Intercalated Layered Double Hydroxide. *J. Catal*. **2022**, 414, 374-384.
12. Simanullang, W. F.; Ma, J. M.; Shimizu, K, I.; Furukawa, S. Silica-Decorated Ni–Zn Alloy as a Highly Active and Selective Catalyst for Acetylene Semihydrogenation. *Catal. Sci. Technol*. **2021**, 11, 4016-4020.
13. Kim K.; Lopez, K. J.; Sun, H.; An, J.; Shim, J.; Park G. Carbon-wrapped Bimetallic Co/Ni Catalysts (C@CoxNi1−x) Derived from Co/Ni-MOF for Bifunctional Catalysts in Rechargeable Zn-Air Batteries, *Bull. Korean Chem. Soc.* **2018**, 39, 1357–1361.